https://doi.org/10.5194/gmd-2020-408
Preprint. Discussion started: 6 January 2021

Geoscientific Model Development
Discussions

MESMO 3: Flexible phytoplankton stoichiometry and refractory DOM

Katsumi Matsumoto, Tatsuro Tanioka, and Jacob Zahn

Department of Earth & Environmental Sciences, University of Minnesota, Minneapolis, Minnesota, USA

Contact: katsumi@umn.edu

Abstract

We describe the third version of Minnesota Earth System Model for Ocean biogeochemistry (MESMO 3), an earth system model of intermediate complexity, with a dynamical ocean, a dynamic-thermodynamic sea ice, and an energy moisture balanced atmosphere. A major feature of Version 3 is the flexible C:N:P ratio for the three phytoplankton functional types represented in the model. The flexible stoichiometry is based on the power law formulation with environmental dependence on phosphate, nitrate, temperature, and light. Other new features include nitrogen fixation, water column denitrification, oxygen and temperature-dependent organic matter remineralization, and $CaCO_3$ production based on the concept of the residual nitrate potential growth. Also, we describe the semi-labile and refractory dissolved organic pools of C, N, P, and Fe that can be enabled in MEMSO 3 as an optional feature. The refractory dissolved organic matter can be degraded by photodegradation at the surface and hydrothermal vent degradation at the bottom. These improvements provide a basis for using MESMO 3 in further investigations of the global marine carbon cycle to changes in the environmental conditions of the past, present, and future.

1. Introduction

Here we document the development of the third version of the Minnesota Earth System Model for Ocean biogeochemistry (MESMO 3). As described for the first two versions (Matsumoto et al., 2008, 2013), MESMO is based on the non-modular version of the Grid ENabled Integrated Earth (GENIE) system model (Lenton et al., 2006; Ridgwell et al., 2007). The computationally efficient ocean-climate model of Edwards and Marsh (Edwards and Marsh, 2005) forms the core of GENIE's physical model. MESMO is an earth system model of intermediate complexity (EMIC), which occupies a midpoint in the continuum of climate models that span high resolution, comprehensive coupled models on one end and box models at the other end (Claussen et al., 2002). MESMO has a 3D dynamical ocean model on a 36 x 36 equal-area horizontal grid with 10° increments in longitude and uniform in the sine of latitude. There are 16 vertical levels. It is coupled to a 2D energy moisture balanced model of the atmosphere and a 2D dynamic and thermodynamic model of sea ice. Thus, MESMO retains important dynamics, which allow for simulations of transient climate change, while still being computationally efficient.

Since the first version, MESMO has continued to be developed chiefly for investigations of ocean biogeochemistry (Table 1). Briefly, in MESMO 1, the main improvements over the predecessor GENIE focused on the biological production and remineralization as well as on the uptake of natural radiocarbon (^{14}C) and anthropogenic transient tracers (Matsumoto et al., 2008). The net primary production (NPP) in MESMO 1 occurred in the top two vertical levels representing the surface 100 m and depended on temperature, nutrients, light, and mixed layer depth (MLD). The nutrient dependence was based on the Michaelis-Menten uptake kinetics of phosphate (PO_4), nitrate (NO_3), and aqueous CO_2. The limiting nutrient was determined by the Liebig's rule of the minimum relative to the fixed uptake stoichiometry of C:N:P=117:16:1. A single generic phytoplankton functional type (PFT) carried out NPP, which was split between particulate organic matter (POM) and dissolved organic matter (DOM) in a globally constant ratio of 1:2. The semi-labile form of the dissolved organic carbon (DOC) was the only form of DOM simulated in MESMO 1. The POM flux across the 100 m level defined the export production. The vertical flux of POM was driven by a fixed rate of sinking and a temperature-dependent, variable remineralization rate.

The main aim of MESMO 2 was a credible representation of the marine silica cycle (Matsumoto et al., 2013). To this end, the set of limiting nutrients (P, N, and C) in MESMO 1 was augmented to include iron (Fe) and silicic acid ($Si(OH)_4$) in MESMO 2 (Table 1). The stable isotope of Si (^{30}Si) was also added as a state variable. The Fe cycle included an aeolian flux of Fe, complexation with organic ligand, and particle scavenging of free Fe. The scavenged Fe that reached the seafloor was removed from the model domain. This burial flux of Fe balanced the aeolian flux at steady state. Also, a new PFT was added in MESMO 2 to represent diatoms. This new "large" PFT was limited by Si and characterized by a high maximum growth rate and large half-saturation constants for the nutrient uptake kinetics. It represented fast and opportunistic phytoplankton that do well under nutrient replete conditions. In comparison, the “small” PFT was characterized with a lower maximum growth rate and smaller half-saturation constants and outperformed the large PFT in oligotrophic subtropical gyres. $CaCO_3$ production was associated with the "small" PFT in MESMO2. The addition of Fe, Si, and the large PFT in MESMO 2 allowed it to have a Fe-dependent, variable Si:N uptake ratio (Hutchins and Bruland, 1998; Takeda, 1998), which is critical to simulate important features of the global ocean Si distribution.

MESMO 1 and 2 were assessed and calibrated by multi-objective tuning and extensive model-data comparisons of transient tracers (anthropogenic carbon, CFCs), deep ocean $\Delta^{14}C$, and nutrients (Matsumoto et al., 2008, 2013). These versions have been employed successfully in a number of studies of global distributions of carbon and carbon isotopes under various conditions of the past, present, and future (Cheng et al., 2018; Lee et al., 2011; Matsumoto et al., 2010, 2020; Matsumoto and McNeil, 2012; Matsumoto and Yokoyama, 2013; Sun and Matsumoto, 2010; Tanioka and Matsumoto, 2017; Ushie and Matsumoto, 2012). Also, MESMO 1 and 2 have participated in model intercomparison projects (Archer et al., 2009; Cao et al., 2009; Eby et al., 2013; Joos et al., 2013; Weaver et al., 2012; Zickfeld et al., 2013).

https://doi.org/10.5194/gmd-2020-408
Preprint. Discussion started: 6 January 2021

In this contribution, we describe the third and latest version of MEMSO with a number of substantial biogeochemical model modifications and new features that bring MESMO up to date with the evolving and accumulating knowledge of the ocean biogeochemical cycle (Table 1). There is no change in the physical model between MESMO 3 and MESMO 2. The most significant new feature of MESMO 3 over the previous versions is the power law formulation of flexible phytoplankton C:N:P ratio. Other new features include additional PFT diazotrophs that carry out N-fixation, water column denitrification, the dependence of organic matter remineralization on the dissolved oxygen (O_2) and temperature, and $CaCO_3$ production based on the concept of the residual nitrate potential growth. Also, we describe the semi-labile DOM for P, N, and Fe (DOP_{sl}, DON_{sl}, and $DOFe_{sl}$), and the refractory DOM for C, P, and N (DOC_r, DOP_r, and DON_r), which can be activated as an optional feature in MESMO 3. Some of these features have been described separately in different publications (Matsumoto et al., 2020; Matsumoto and Tanioka, 2020; Tanioka and Matsumoto, 2017, 2020a). This work consolidates the descriptions of all these features in a single publication.

2. Model Description

Here we present the full set of biogeochemical equations of MESMO 3 as well as key model parameters (Table 2). We describe only the biogeochemical source and sink terms and omit the physical (advective and diffusive) transport terms that are calculated by the ocean circulation model. We discuss the production terms first, followed by remineralization terms, followed by conservation equations that incorporate both terms.

2.1 Phytoplankton Nutrient Uptake

NPP occurs in the top two vertical levels of the ocean domain above the fixed compensation depth (z_c) of 100 m. Key parameter values are given in Table 2a. Nutrient uptake by phytoplankton type i (Γ_i) depends on the optimal nutrient uptake timescale (τ_i), nutrients, temperature (T), irradiance (I), and mixed layer depth (z_{ml}):

$$\Gamma_i = \frac{1}{\tau_i} \cdot F_{N,i} \cdot F_T \cdot F_I \cdot max\left\{1, \frac{z_c}{z_{ml}}\right\} \qquad 1$$

Subscript i refers to PFT (i =1: eukaryotes, i =2: cyanobacteria, i = 3: diazotrophs). The nutrient dependence $F_{N,i}$ is given by Liebig's law of minimum combined with Michael-Menten uptake kinetics of limiting nutrients: PO_4, NO_3, CO_2, (aq), total dissolved iron (sum of free iron and ligand-bound iron; FeT=Fe'+FeL), and silicic acid ($Si(OH)_4$):

$$F_{N,i} = min\left(\frac{[PO_4]}{[PO_4]+K_{PO_4,i}} \cdot [PO_4], \frac{[NO_3]}{[NO_3]+K_{NO_3,i}} \cdot [NO_3] \cdot Q_{N,i}{}^{-1}, \frac{[CO_2(aq)]}{[CO_2(aq)]+K_{CO_2,i}} \cdot [CO_2(aq)] \cdot Q_{C,i}{}^{-1}, \frac{[FeT]}{[FeT]+K_{FeT,i}} \cdot [FeT] \cdot Q_{Fe,i}{}^{-1}, \frac{[Si(OH)_4]}{[Si(OH)_4]+K_{Si(OH)_4}} \cdot [Si(OH)_4] \cdot Q_{Si}{}^{-1}\right), \qquad 2$$

where $K_{X,i}$ is the half-saturation concentration of nutrient X for PFT i. Only eukaryotes (i=1) are limited by $Si(OH)_4$. Diazotrophs (i = 3) are not limited by NO_3. Nutrient uptake Γ is based on the master nutrient variable P, and all other nutrient uptake is related to Γ by the uptake stoichiometry $Q_{X,i}$, where X is N, Fe, Si, or C. For example, $Q_{C,i} = \frac{1}{[P:C]_i}$ for PFT i. Thus, $Q_{c,i}$ is numerically equivalent to C:P for PFT i, but we write the equations in terms of P:C for numerical stability and convenience. The $Q_{X,i}$ ratios represent the flexible phytoplankton uptake stoichiometry and describe more fully in the following section 2.2.

The temperature dependence F_T of Equation 1 is given by:

$$F_T = \frac{T(\,^\circ C) + 2}{T(\,^\circ C) + 10} \qquad 3$$

which is analogous to the commonly used $Q_{10} = 2$ relationship. Light limitation F_I of Equation 1 is described by a hyperbolic function:

$$F_T = \frac{I}{I + 20} \qquad (4)$$

where I is the seasonally variable solar short-wave irradiance in W m^{-2}. Light is attenuated exponentially from the ocean surface with a 20 m depth scale.

Nutrient uptake in Equation 1 has a dependence on z_{ml}, which is diagnosed using the σ_t density gradient criterion (Levitus, 1982). Following the Sverdrup (1953) model of the spring bloom, Equation 1 allows for the shoaling of z_{ml} relative to z_c to enhance nutrient uptake.

2.2 Phytoplankton uptake stoichiometry

As noted above, all nutrients and O_2 are related to the main model currency P by $Q_{X,i}$. We describe three different, mutually exclusive formulations in this section. The standard formulation is the power law model (Matsumoto et al., 2020; Tanioka and Matsumoto, 2017). The other two (Linear model and Optimality-based model of stoichiometry) are alternative formulations that have been coded, and the user can activate them (one at a time) in place of the power law formulation. However, the alternative formulations are not calibrated. Key parameter values are given in Table 2b for the power law formulation.

2.2.1 Power law model of stoichiometry

The uptake P:C and N:C ratios are calculated using the power-law formulation as a function of ambient concentrations of phosphate [PO_4], nitrate [NO_3], temperature (T), and Irradiance (I):

https://doi.org/10.5194/gmd-2020-408
Preprint. Discussion started: 6 January 2021

$$[P:C]_i = [P:C]_{0,i} \cdot \left(\frac{[PO_4]}{[PO_4]_0}\right)^{s^{P:C}_{PO_4,i}} \cdot \left(\frac{[NO_3]}{[NO_3]_0}\right)^{s^{P:C}_{NO_3,i}} \cdot \left(\frac{T}{T_0}\right)^{s^{P:C}_{T,i}} \cdot \left(\frac{I}{I_0}\right)^{s^{P:C}_{I,i}} \tag{5}$$

$$[N:C]_i = [N:C]_{0,i} \cdot \left(\frac{[PO_4]}{[PO_4]_0}\right)^{s^{N:C}_{PO_4,i}} \cdot \left(\frac{[NO_3]}{[NO_3]_0}\right)^{s^{N:C}_{NO_3,i}} \cdot \left(\frac{T}{T_0}\right)^{s^{N:C}_{T,i}} \cdot \left(\frac{I}{I_0}\right)^{s^{N:C}_{I,i}} \tag{6}$$

Equations 5 and 6 are the power-law equations that calculate the change in P:C and N:C for fractional changes in environmental drivers relative to the reference P:C and N:C, respectively (Matsumoto et al., 2020; Tanioka and Matsumoto, 2017). The exponents are the sensitivity factors determined by a meta-analysis (Tanioka and Matsumoto, 2020a). Subscript "0" indicates the reference values (Table 2b).

The P:C and N:C ratios from Equations 5 and 6 can then be converted to $Q_{N,i}$ and $Q_{C,i}$ for use in Equation 2.

$$Q_{C,i} = \frac{1}{[P:C]_i} \tag{7}$$

$$Q_{N,i} = \frac{1}{[P:N]_i} = \frac{[N:C]_i}{[P:C]_i} \tag{8}$$

2.2.2 Linear model of stoichiometry by Galbraith & Martiny

A much simpler, alternative formulation for P:C and N:C is the model of Galbraith & Martiny (2015) where P:C is a linear function of $[PO_4]$ (in µM), and N:C is a Holling type 2 functional form with a frugality behavior only at very low $[NO_3]$ (in µM). The same P:C and N:C values are applied to all three PFTs.

$$[P:C] = \frac{6.9 \cdot [PO_4] + 6.0}{1000} \quad 9$$

$$[N:C] = 0.125 + \frac{0.03 \cdot [NO_3]}{0.32 + [NO_3]} \quad 10$$

2.2.3 Optimality-based model of stoichiometry

The optimality-based model of phytoplankton growth is based on the chain model, which connects the cellular P, N, and C acquisition by a chain of limitations, where the P quota limits N assimilation and the N quota drives carbon fixation (Pahlow et al., 2013; Pahlow and Oschlies, 2009, 2013). Resource-allocation of cellular P, N, and C among different cellular compartments are derived from balancing energy gain from gross carbon fixation and energy loss due to nutrient acquisition and light-harvesting. The optimality-based model by Pahlow et al. (2013) computes C:N and C:P as a function of nutrient availability (PO_4 and NO_3), irradiance, and day length. Temperature dependence was added by Arteaga et al. (2014) following the simple logarithmic temperature dependence on maximum nutrient uptake rate following (Eppley, 1972).

Different versions of this optimality-based model have previously been successfully implemented in global ocean biogeochemical models, such as the Pelagic Interactions Scheme for Carbon and Ecosystem Studies (PISCES) (Kwiatkowski et al., 2018, 2019) and the University of Victoria Earth System Model (UVIC) (Chien et al., 2020; Pahlow et al., 2020). However, as we are not describing any results in this paper, we will only mention here that there is an option to calculate C:N:P using this stoichiometry model in MESMO 3. The full description of the optimality-based stoichiometry model and its parameter calibration are presented specifically for the UVic model elsewhere (Chien et al., 2020; Pahlow et al., 2020).

2.2.4 Stoichiometry of iron and silica

Iron uptake stoichiometry $Q_{Fe,i}$ is calculated as a function of FeT following the power-law formulation of Ridgwell (2001). Key parameter values are given in Table 2c.

$$Q_{Fe,i} = [Fe:P]_i = [Fe:C]_i \cdot Q_{C,i} \qquad 11$$

$$[Fe:C]_i = 1.0/([C:Fe]_{min,i} + [C:Fe]_{ref,i} \cdot [FeT]^{-s^{Fe:C_i}}) \qquad 12$$

For all PFTs, the power law exponent $s^{Fe:C}$ in Equation 12 is -0.65. The allowable Fe:C ratio is bounded at the low end by the hard-bound minimum Fe:C of 1:220,000. The scaling constant or $[C:Fe]_{ref,i}$ is set differently for PFTs, with eukaryotes having a higher base $[C:Fe]_{ref,i}$ than cyanobacteria and diazotrophs (115,623:1 and 31,805:1, respectively). The high end of the allowable Fe:C ratio is bounded by $[C:Fe]_{min,i}$ (i.e., maximim Fe:C) of 15,000:1 for eukaryotes and 20,000:1 for cyanobacteria/diazotrophs. These parameters directly follow Ridgwell (2001), who fitted power-law functions to the experimental data (Sunda and Huntsman, 1995).

Silica uptake stoichiometry by eukaryotes Q_{Si} is a power law of total dissolved iron [FeT] and increases with a decrease in [FeT] (Brzezinski, 2002). The power law exponent $s^{Si:N}$ is set to 0.7. The Si:N ratio is limited to a maximum of 18 and a minimum of 1.

$$Q_{Si} = [Si:P] = [Si:N] \cdot Q_{N,1} \qquad 13$$

$$[Si:N] = min\left([Si:N]_{max}, max\left([Si:N]_{min}, \left(\frac{[FeT]}{0.5\ nmol\ kg^{-1}}\right)^{-s^{Si:N}}\right)\right) \qquad 14$$

O_2 liberated by phytoplankton during photosynthesis per PO_4 consumed ($Q_{-O_{2},i}$) is calculated from the uptake C:P and N:P ratios (Tanioka and Matsumoto, 2020b):

$$Q_{-O_{2},i} = 1.1Q_{C,i} + 2Q_{N,i} \qquad 15$$

2.3 Production of POM and DOM

In the top 100 m of the model domain, where phytoplankton P uptake occurs (i.e., $\Gamma_i > 0$, see section 2.1), NPP is produced and immediately routed to POM and DOM pools (Figure 1). The production fluxes of POM, DOM_{sl}, and DOM_r from NPP are given as Jprod. Here we write the equations in terms of P, which is the mater nutrient variable:

$$Jprod_{POP_i} = (1 - fDOM) \cdot \Gamma_i \tag{16}$$

$$Jprod_{DOP_{sl}} = \sum_i (1 - fDOM_r) \cdot fDOM \cdot \Gamma_i \tag{17}$$

$$Jprod_{DOP_r} = \sum_i fDOM_r \cdot fDOM \cdot \Gamma_i \tag{18}$$

The term fDOM denotes the fraction of NPP that is routed to DOM as opposed to POM. Likewise, $fDOM_r$ is the fraction of DOM that is routed to DOM_r as opposed to DOM_{sl}. The value of $fDOM_r$ is not well known but estimated to be ~1% (Hansell, 2013), which we tentatively adopt in MESMO 3. If DOM_r is not selected in the model run, $fDOM_r = 0$. In previous versions of MESMO, fDOM was assigned a constant value of 0.66. In reality, a large variability is observed for this ratio, ranging from 0.01-0.2 in temperate waters to 0.1-0.7 in the Southern Ocean (Dunne et al., 2005; Henson et al., 2011; Laws et al., 2000). In MESMO 3, fDOM is calculated as a function of the ambient temperature following Laws et al. (2000):

$$fDOM = 1.0 - min\left(0.72, max\left(0.04, 0.62 - 0.02 \cdot T(°C)\right)\right) \tag{19}$$

This formulation gives low export efficiency (i.e., high fDOM) in the warmer regions compared to the colder high latitude regions. We impose fixed fDOM upper and lower bounds of 0.96 and 0.28, respectively, as estimated from a previous study (Dunne et al., 2005).

In MEMSO 3, a new DOM production pathway below the production layer is available as an option. In previous MESMO versions, sinking POM was respired in the water column with the loss of O_2 directly to the dissolved inorganic forms (i.e., POC-->DIC, POP-->PO_4, and POP-->NO_3). In the new "deep POC split" pathway, sinking POM is simply broken down into DOM without the loss of O_2 (Figure 1). If DOM_r is selected in the model, the broken down POM is further routed to both DOM_{sl} and DOM_r according to $fDOM_r$. If not, all of the broken down POM is converted to DOM_{sl}. Thus, when the deep POC split is activated, the presence of DOM in the deep ocean can be accounted for by *in situ* production of DOM and DOM_r in addition to DOM transport from the surface. Thus, the deep POC split pathway offers an alternative means to control deep ocean DOM distribution.

2.4 Production of $CaCO_3$ and opal by eukaryotes

In MESMO 2, opal production was associated with the large PFT and $CaCO_3$ production was associated with the "small" PFT. We recognize that coccolithophorids and diatoms, which are the producers of these biogenic tests, are both eukaryotes. Therefore, in MEMSO 3, we associate both $CaCO_3$ and opal production with the POM production by the same eukaryote PFT ($Jprod_{POM1}$) :

$$Jprod_{CaCO3} = r^{CaCO_3:POC} \cdot Jprod_{POM1} \cdot Q_{C,1} \tag{20}$$

$$Jprod_{opal} = Jprod_{POM1} \cdot Q_{Si} \tag{21}$$

The concept of the residual nitrate potential growth (RNPG) (Balch et al., 2016) is useful in allowing competition between diatoms and non-siliceous phytoplankton within the same PFT (Matsumoto et al., 2020). Typically, in the real ocean, non-Si phytoplankton are able to grow faster and dominate the community if Si concentration is low and diatom growth is Si limited. Otherwise, diatoms are more competitive, as they have higher intrinsic growth rates. The RNPG index recasts the ambient concentrations of NO_3 and $Si(OH)_4$ into potential algal growth rates:

$$RNPG = \frac{[NO_3]}{[NO_3] + K_{NO_3,1}} - \frac{[Si(OH)_4]}{[Si(OH)_4] + K_{Si(OH)_4}} \tag{22}$$

If RNPG is more positive, the index indicates that nitrate-dependent growth exceeds silicate-dependent growth. Thus, non-Si phytoplankton are more competitive, and this leads to higher $CaCO_3$ production. On the other hand, a more negative RNPG implies that silicate limitation for diatoms is relieved, leading to enhanced diatom growth and reduced $CaCO_3$ production. The RNPG index is incorporated in the calculation of the rain ratio $r^{CaCO_3:POC}$ presented in Equation 20 as:

$$r^{CaCO_3:POC} = r_0^{CaCO_3:POC} \cdot (\Omega - 1)^{\eta} \cdot min(1, max(0.1, RNPG)) \cdot k_{T,CaCO_3} \tag{23}$$

Equation 23 indicates the base rain ratio $r_0^{CaCO_3:POC}$ (set to 0.30) is also modified by the carbonate ion saturation state Ω by η (set to 1.28) by as well as by temperature (see Ridgwell et al. (2007) and references therein):

$$\Omega = \frac{[Ca^{2+}][CO_3^{2-}]}{K_{sp}} \tag{24}$$

$$k_{T,CaCO_3} = min\left(1.0, \frac{T(^\circ C) + 2}{T(^\circ C) + 8}\right) \tag{25}$$

K_{sp} is the solubility product of $CaCO_3$. The temperature dependency of $CaCO_3$ formation ($k_{T,CaCO_3}$) is similar to that of Moore et al. (2004) where warmer temperatures favor the growth of carbonate-bearing phytoplankton.

2.5 Remineralization of POM and DOM

Once produced, both POM and DOM undergo remineralization throughout the water column. Key remineralization parameter values are given in Table 2d. Previously, POM remineralization had a temperature dependence and decayed exponentially with depth

(Yamanaka et al., 2004). In MESMO 3, we incorporate an additional dependency on dissolved oxygen following Laufkötter et al. (2017):

$$R_{POM_i} = V_{POM} \cdot e^{k_R \cdot T \cdot \frac{[O_2]}{[O_2]+K_{O_2}}} \cdot [POM_i] \tag{26}$$

V_{POM} is the base remineralization rate, parameter k_R expresses the temperature sensitivity of remineralization, and K_{O_2} is half-saturation constant for oxygen-dependent remineralization. When the sediment model is not coupled, any POM that reaches the seafloor dissolves completely to its inorganic form and is returned to the overlying water.

In MESMO 3, all forms of semi-labile DOM remineralize at the same rate. It is represented by τ_{sl}, the inverse of the time scale of DOM_{sl} decay, which has been estimated previously to be ~1.5 years (Hansell, 2013):

$$R_{DOM_{sl}} = \tau_{sl} \cdot [DOM_{sl}] \tag{27}$$

All forms of DOM_r also remineralize at the same rate in MESMO 3. In total, there are three optional, additive sinks of DOM_r in the model: slow background decay, photodegradation, and degradation via hydrothermal vents (Figure 1). Observations clearly indicate that the ^{14}C age of deep ocean DOC_r is 10^3 years (e.g., Druffel et al., 1992), much older than $DI^{14}C$. Also, the deep ocean DOC_r concentration decreases modestly along the path of the deep water from the deep North Atlantic to the deep North Pacific (Hansell and Carlson, 1998). Thus, it is understood that there is a slow DOM_r background decay in the deep ocean. We represent this process with τ_{bg}, which is the inverse of the background decay time scale, estimated to be ~16,000 years (Hansell, 2013).

Observations to date indicate that photodegradation is a major sink of DOM_r (e.g., Mopper et al., 1991). This process is believed to convert DOM_r that is upwelled from the ocean interior into the euphotic zone into more labile forms of DOM. We represent photodegradation with τ_{photo}, the inverse of the decay time scale, estimated to be ~70 years (Yamanaka and Tajika, 1997).

Finally, observations of DOM emanating from different types of hydrothermal vents indicate that they have variable impacts on the deep sea DOM_r (Lang et al., 2006). However, the off-axis vents circulate far more seawater through the fractured oceanic crust than the high temperature and diffuse vents and thus believed to determine the overall impact of the vents on the deep sea DOM_r as a net sink (Lang et al., 2006). Here we assume simply that seawater that circulates through the vents loses all DOM_r (i.e., $1/\tau_{vent} < \Delta t$, where Δt is the biogeochemical model time step of 0.05 year). This means that the more seawater circulates through the vents, the more DOM_r is removed: the total removal rate depends on the vent flux of seawater H_{flux}. We implement the vent degradation of DOM_r in MESMO 3 by first identifying the wet grid boxes located immediately above known mid-ocean ridges. We then distribute the annual global H_{flux} of 4.8×10^{16} kg yr^{-1} (Lang et al., 2006) equally among those ridge-associated grid boxes. The grid cells contain a mass of seawater much greater than the mass that circulates through vents in Δt (10^{21} kg vs. 10^{13} kg). Therefore, the seawater mass in the vent grid cells that does not circulate through the vents in Δt is subject only to background degradation in MESMO 3.

The three DOM_r sinks are not mutually exclusive. They can thus be combined to yield the total DOM_r remineralization rate:

$$R_{DOM_r} = (\tau_{bg} + \tau_{photo} + \tau_{vent} \cdot \frac{SW_{flux\_local}}{SW_{grid}}) \cdot [DOM_r] \qquad 28$$

where SW_{flux_local} is the mass of seawater that circulates through the vents in each grid box in Δt, and SW_{grid} is the total mass of seawater in the same grid box.

The amount of O_2 respired as a result of these POM and DOM remineralization processes is related to the organic carbon pools by the respiratory quotients of POC and DOC, $r_{-O_2:POC}$

and $r_{-O_2:DOC}$, respectively. These are molar ratios of O_2 consumed per unit organic carbon respired. They are variable and calculated from the ambient POM and DOM concentration (Tanioka and Matsumoto, 2020b):

$$r_{-O_2:POC} = 1.1 + \frac{2[PON]}{[POC]} \quad (29)$$

$$r_{-O_2:DOC} = 1.1 + \frac{2[DON]}{[DOC]} \quad (30)$$

2.6 Remineralization of $CaCO_3$ and opal

Remineralization of $CaCO_3$ and opal particles occurs as they sink through the water column and remains the same as in MESMO 2. Key parameter values are given in Table 2d. Remineralization of $CaCO_3$ is a function of temperature similar to that of particulate organic matter remineralization but without oxygen dependency. The temperature dependence term k_R modifies the base remineralization rate V_{CaCO_3}:

$$R_{CaCO_3} = V_{CaCO_3} \cdot e^{k_R \cdot T} \cdot [CaCO_3] \quad (31)$$

Opal remineralization in the water column follows Ridgwell et al. (2002). The rate of opal remineralization R_{opal} is given by the product of normalized dissolution rate (r_{opal}), base opal dissolution rate (k_{opal}), and opal concentration [opal]:

$$R_{opal} = r_{opal} \cdot k_{opal} \cdot [opal] \quad (32)$$

$$r_{opal} = 0.16 \cdot \left(1 + \frac{T(℃)}{15}\right) \cdot u_{opal} + 0.55 \cdot \left(\left(1 + \frac{T(℃)}{400}\right)^4 \cdot u_{opal}\right)^{9.25} \quad (33)$$

$$u_{opal} = \frac{[Si(OH)_4]_{eq} - [Si(OH)_4]}{[Si(OH)_4]_{eq}} \quad (34)$$

r_{opal} is a function of temperature (T) and the degree of under-saturation (u_{opal}), which in turn is calculated from the ambient $[Si(OH)_4]$ and $[Si(OH)_4]$ at equilibrium. The equilibrium concentration is a function of ambient temperature:

$$log_{10}\left([Si(OH)_4]_{eq}\right) = 6.44 - \frac{968}{T(K)} \qquad 35$$

Without the sediment module of MESMO activated, both $CaCO_3$ and opal particles that reach the seafloor are completely dissolved back to inorganic forms.

2.7 Conservation of organic matter and biogenic tests

The time rate of change of the biogenic organic matter and tests are given by the sum of the production terms (i.e., sources) and the remineralization terms (i.e., sinks). The circulation-related transport terms are omitted as noted above, but the vertical transport due to particle sinking is included here. The sinking speed w is the same for all particles. The sum of POM_i of all the PFTs give the total POM concentrations:

$$\frac{\partial [POP]_i}{\partial t} = Jprod_{POP_i} - \frac{\partial}{\partial z}(w[POP]_i) - R_{POP,i} \qquad 36$$

$$\frac{\partial [POC]_i}{\partial t} = Jprod_{POP_i} \cdot Q_{C,i} - \frac{\partial}{\partial z}(w[POC]_i) - R_{POC,i} \qquad 37$$

$$\frac{\partial [PON]_i}{\partial t} = Jprod_{POP_i} \cdot Q_{N,i} - \frac{\partial}{\partial z}(w[PON]_i) - R_{PON,i} \qquad 38$$

$$\frac{\partial [POFe]_i}{\partial t} = Jprod_{POP_i} \cdot Q_{Fe,i} - \frac{\partial}{\partial z}(w[POFe]_i) - R_{POFe,i} \qquad 39$$

$$[POM] = \sum_i [POM]_i \qquad 40$$

The time rate of change of $CaCO_3$ and opal is expressed in much the same way as POM:

https://doi.org/10.5194/gmd-2020-408
Preprint. Discussion started: 6 January 2021

$$\frac{\partial[CaCO_3]}{\partial t} = Jprod_{CaCO3} - \frac{\partial}{\partial z}(w[CaCO_3]) - R_{CaCO_3} \qquad 41$$

$$\frac{\partial[opal]}{\partial t} = Jprod_{opal} - \frac{\partial}{\partial z}(w[opal]) - R_{opal} \qquad 42$$

The DOM pools have the production and remineralization terms without the particle sinking term:

$$\frac{\partial[DOP_{sl}]}{\partial t} = Jprod_{DOP_{sl}} - R_{DOP_{sl}} \qquad 43$$

$$\frac{\partial[DON_{sl}]}{\partial t} = Jprod_{DON_{sl}} - R_{DON_{sl}} \qquad 44$$

$$\frac{\partial[DOC_{sl}]}{\partial t} = Jprod_{DOC_{sl}} - R_{DOC_{sl}} \qquad 45$$

$$\frac{\partial[DOFe_{sl}]}{\partial t} = Jprod_{DOFe_{sl}} - R_{DOFe_{sl}} \qquad 46$$

$$\frac{\partial[DOP_r]}{\partial t} = Jprod_{DOP_r} - R_{DOP_r} \qquad 47$$

$$\frac{\partial[DON_r]}{\partial t} = Jprod_{DON_r} - R_{DON_r} \qquad 48$$

$$\frac{\partial[DOC_r]}{\partial t} = Jprod_{DOC_r} - R_{DOC_r} \qquad 49$$

2.8 Conservation of inorganic nutrients

The time rate of change of the inorganic nutrients have organic carbon production as sink terms and remineralization as source terms. The production terms (J_{prod}) are zero below the upper ocean production layer. Nutrients generally have a unit of μmol element kg^{-1}, except for iron, whose unit is nmol Fe kg^{-1}.

$$\frac{\partial[PO_4]}{\partial t} = -\sum_i \Gamma_i + \sum_i R_{POP,i} + R_{DOP_{sl}} + R_{DOP_r} \tag{50}$$

$$\frac{\partial[NO_3]}{\partial t} = -\sum_i \Gamma_i \cdot Q_{N,i} + \sum_i R_{PON,i} + R_{DON_{sl}} + R_{DON_r} + Fix_N - Den_N \tag{51}$$

$$\frac{\partial[DIC]}{\partial t} = -\left(\sum_i \Gamma_i Q_{C,i} + Jprod_{CaCO3}\right) + \sum_i R_{POC,i} + R_{DOC_{sl}} + R_{DOC_r} + R_{CaCO_3} + F_{gas,CO_2} \tag{52}$$

$$\frac{\partial[ALK]}{\partial t} = -\left(2 \cdot Jprod_{CaCO3} - \sum_i \Gamma_i Q_{N,i}\right) - \sum_i R_{PON,i} - R_{DON_{sl}} - R_{DON_r} - Fix_N + Den_N + 2 \cdot R_{CaCO_3} \tag{53}$$

$$\frac{\partial[FeT]}{\partial t} = -\sum_i \Gamma_i Q_{Fe,i} + \sum_i R_{POFe,i} + R_{DOFe_{sl}} + R_{POM_{Fe}} + Aeolian_{Fe} \tag{54}$$

$$\frac{\partial[Si(OH)_4]}{\partial t} = -Jprod_{opal} + R_{opal} \tag{55}$$

$$\frac{\partial[O_2]}{\partial t} = \sum_i \Gamma_i \cdot Q_{-O_2,i} - \left(r_{-O_2:DOC} \cdot \left(R_{DOC_{sl}} + R_{DOC_r}\right) + \sum_i r_{-O_2:POC,i} \cdot R_{POC,i}\right) + 1.25\ Den_N + F_{gas,O_2} \tag{56}$$

In Equation 51, Fix_N is the N-fixation carried out by diazotrophs, and Den_N is the water column denitrification. There is an air-sea gas exchange term F_{gas} in Equations 52 and 56 for gaseous CO_2 and O_2, respectively. In Equation 53, alkalinity increases with decreasing nitrate concentrations and increasing $CaCO_3$ dissolution. Equation 54 contains R_{POMFe}, which is an iron source that represents remineralization of the Fe' scavenged by sinking particles. These terms are explained in the following sections.

2.9 Prognostic nitrogen cycle

Biological production by diazotrophs is stimulated when the ambient NO_3 is low. Nitrogen fixed by diazotrophs during their growth is added to the marine NO_3 pool. The prognostic nitrogen fixation model employed here is similar to that used in the HAMOCC biogeochemical module (Paulsen et al., 2017):

$$Fix_N = \Gamma_3 \cdot Q_{N,3} \cdot I_{NO_3}\ , \qquad 57$$

$$I_{NO_3} = \left(1.0 - \frac{[NO_3]^2}{{K_{N_2}}^2 + [NO_3]^2}\right), \qquad 58$$

where Fix_N is the nitrogen fixation rate and I_{NO_3} is the nitrate dependency term in quadratic Michaelis-Menten kinetics form with the half-saturation constant K_{N_2}. See Table 2e for the values related to the N cycle.

Water-column denitrification is formulated in an approach similar to that of the original GENIE model (Ridgwell et al., 2007), in which 2 moles of NO_3 are converted to 1 mole of N_2 and liberating 2.5 moles of O_2 as a byproduct:

$$2NO_3^- + 2H^+ \rightarrow 2.5O_2 + N_2 + H_2O \qquad 59$$

Denitrification takes place in grid boxes, in which O_2 concentration is below a threshold concentration ($O_{2,def}$) and is stimulated if the total global inventory of NO_3 relative to PO_4 is high. In other words, denitrification can effectively act as negative feedback to nitrogen fixation. The threshold O_2 concentration ($O_{2,def}$) takes the minimum of the hard-bound O_2 threshold concentration ($O_{2,crit}$) and the NO_3 to PO_4 ratio, scaled by a parameter k_D. The parameters $O_{2,crit}$ and k_D are calibrated to give the global denitrification rate of roughly 100 Tg N yr^{-1}, which balances the total nitrogen fixation rate in the model.

$$Den_N = 0.8\,[yr^{-1}] \cdot max\left(([O_2]_{def} - [O_2]), 0\right) \qquad 60$$

$$[O_2]_{def} = min\left(O_{2,crit}, k_D \cdot \frac{[NO_3]_{inventory}}{[PO_4]_{inventory}}\right) \qquad 61$$

2.10 Prognostic iron cycle

The iron cycle in MESMO 3 remains the same as in MESMO 2. Key parameter values are given in Table 2e. The two species of dissolved iron (Fe' and FeL) are partitioned according to the following equilibrium relationship:

$$K_{ligand} = \frac{[FeL]}{[Fe'] \cdot [L]} \qquad 62$$

where [L] is the ligand concentration, and K_{ligand} is the conditional stability constant. The sum of ligand and FeL is set at a constant value of 1 nmol kg^{-1} everywhere. Iron is introduced into the model domain by a constant fraction (3.5 weight %) of aeolian dust deposition at the surface (F_{in}) following the prescribed modern flux pattern (Mahowald et al., 2006) with constant solubility (β):

$$S_{Fe} = \beta \cdot F_{in} \qquad 63$$

Particle-scavenged iron POM_{Fe} (note the difference from POFe) is produced below the productive layer when sinking POM scavenges Fe$'$ to sinking POM:

$$J_{Fe} = -\tau_{sc} \cdot K_o \cdot [POC]^{0.58} \cdot [Fe'] \qquad 64$$

where τ_{sc} and K_o and are empirical parameters that determine the strength of scavenging. Remineralization of Fe scavenged to POM (POM_{Fe}) is identical in form to that of POM remineralization:

$$R_{POM_{Fe}} = V_{POM} \cdot e^{k_R T \cdot \frac{[O_2]}{[O_2]+K_{O_2}}} \cdot [POM_{Fe}] \tag{65}$$

The conservation equation of the particle scavenged iron is thus expressed as :

$$\frac{\partial [POM_{Fe}]}{\partial t} = J_{Fe} - \frac{\partial}{\partial z}(w[POM_{Fe}]) - R_{POM_{Fe}} \tag{66}$$

Any scavenged iron that escapes remineralization in the water column reaching the seafloor is removed from the model domain in order to keep the total Fe inventory at a steady state.

2.11 Air-sea gas Exchange

The air-sea gas exchange formulation remains the same as in MESMO 2 and follows Ridgwell et al. (2007). It is the function of gas transfer velocity, the ambient dissolved gas concentration, and saturation gas concentration. The flux of CO_2 and O_2 gases across the air-sea interface is given by:

$$F_{gas,CO_2} = k \cdot \rho \cdot ([CO_2]_{sat} - [CO_2]) \cdot (1 - A) \tag{67}$$

$$F_{gas,O_2} = k \cdot \rho \cdot ([O_2]_{sat} - [O_2]) \cdot (1 - A) \tag{68}$$

where k is the gas transfer velocity, ρ is the density of seawater, $[CO_2]_{sat}$ and $[O_2]_{sat}$ are saturation concentrations, and A is the fractional ice-covered area that is calculated by the physical model. Gas transfer velocity k is a function of wind speed (u) following Wanninkhof (1992) where Sc is the Schmidt Number for a specific gas:

https://doi.org/10.5194/gmd-2020-408
Preprint. Discussion started: 6 January 2021

$$k = 0.31 \cdot u^2 \cdot \left(\frac{Sc}{660}\right)^{-0.5} \qquad 69$$

3 Results and Discussion

All new results from MESMO 3 presented here are from the steady state. The "standard" MESMO 3 has the power law model of flexible stoichiometry but no DOM$_r$. The results from the standard model (hereafter just MESMO 3) are presented in Section 3.1, and the results from the DOM$_r$-enabled model are presented in Section 3.2. In Table 3, we summarize and compare key biogeochemical diagnostics from MESMO 3 against those from MESMO 2 and available observational constraints. The global NPP, as well as global export production of POC, DOC, and opal, are comparable or somewhat lower in MESMO 3 than MESMO 2. For example, the global opal export production is nearly the same at 128-130 Tmol Si y^{-1}, while the global POC export is 9.4 Pg C y^{-1} in MESMO 3 and 11.9 Pg C y^{-1} in MESMO 2. One reason for the lower POC export in the new model is that the global mean, production-layer fDOM, which was 0.66 everywhere in MESMO 2, increased to 0.71 in MESMO 3.

Before discussing the new features of MESMO 3, we note that the new model does just as well if not better than MESMO 2 in terms of the global distributions of PO_4, NO_3, O_2, $Si(OH)_4$, and FeT (Supplemental Figures S1, S2, S3, S4, and S5). Overall there is a stronger nutrient depletion in the new model. For example, the surface concentrations of PO_4 and NO_3 of the two models are both depleted in the subtropical gyres but more so in MESMO 3, which is more in line with the World Ocean Atlas (Figure S1). The spatial pattern of POC export that drives this surface nutrient pattern is similar in the two models (Figure S2). There is a marked improvement in the subsurface distribution of O_2 in MESMO 3 over MESMO 2. Whereas the depth of the oxygen minimum was ~300 m in MEMOS 2, it is ~1000 m in both MESMO 3 and the World Ocean Atlas (Figure S3). The O_2 improvement comes in part from adjusting the particle sinking speed and fDOM. As for $Si(OH)_4$, MESMO 3 preserves MESMO 2's surface depletion in much of the world ocean except in the North Pacific and Southern Ocean (Figure S4). This is a feature captured by $Si^*<0$ ($Si^*=[Si(OH)_4]-[NO_3]$) in observations (Sarmiento et al., 2004) and simulated previously by MESMO 2 and now MESMO 3. Finally, surface FeT is also depleted more strongly in MESMO 3 over MESMO2, except the North Atlantic, where aeolian deposition of dust from the Sahara maintains a steady Fe supply (Figure S5).

3.1 Novel features of MESMO 3

An important new feature of MESMO 3 is the representation of the primary producers by three PFTs (Figure 2). The eukaryotes are characterized by the highest maximum growth rate and high half-saturation constants. Thus, the eukaryotes are more dominant than the other PFTs in the more eutrophic waters of the equatorial and polar regions (Figure 2a). The cyanobacteria have smaller half-saturation constants and thus are more dominant in the oligotrophic subtropical gyres (Figure 2c). The diazotrophs do not have NO_3 limitation but have the lowest maximum growth rate. Thus it is much lower in abundance than the other two PFTs generally, and outcompeted in transient blooms and thus excluded in higher latitudes (Figure 2e). Figure 1 also indicates that all three PFTs show Fe limitation in the Southern Ocean. Outside the Southern Ocean, the eukaryotes are primarily limited by $Si(OH)_4$ (Figure 1b), while the cyanobacteria is limited by NO_3 (Figure 2d). The diazotrophs are limited by iron in much of the world ocean except in the Atlantic basin (Figure 2f), where surface PO_4 is strongly depleted in both observations (Mather et al., 2008) and in our model (Figure S1).

Figure 3 illustrates the influence of the RNPG index, which was implemented in MESMO 3 to allow for the effect of competition between diatoms and coccolithophores within the same PFT (Equations 22 and 23). The eukaryote NPP (Figure 3a) is effectively split into two parts: one is associated with diatoms and opal production (Figure 3b), and the other is associated with coccolithophores and $CaCO_3$ production (Figure 3c). According to the RNPG index, opal production is simulated more in the higher latitudes of the Southern Ocean and the North Pacific, where surface $[Si(OH)_4]$ is abundant. Elsewhere, $CaCO_3$ production is relatively larger. The decoupling is prominent in the North Indian. Note that the spatial pattern of $CaCO_3$ production is quite different in MEMOS 3 (Figure 3c) and MESMO 2 (Figure 3d), because $CaCO_3$ production was associated in MESMO 2 with the "small" PFT, which corresponds to the cyanobacteria PFT in MESMO 3.

The global pattern of the mean C:P uptake ratio in the production layer is shown in Figure 4. Consistent with observations (Martiny et al., 2013), the simulated C:P ratio of the phytoplankton community is elevated in the oligotrophic subtropical gyres and low in the eutrophic polar waters (Figure 4a). The community C:P ratio exceeds 200 in the gyres and reaches as low as 40-50 in the Southern Ocean. The community C:P has contributions from both physiological effects (i.e., environment acts on each PFT's C:P ratio) and taxonomic effects (i.e., the shift in the community composition changes the weighting of each PFT's C:P ratio). Figure 4b shows that the community C:P is high in oligotrophic gyres partly because cyanobacteria and to a lesser extent diazotrophs dominate the community, and their C:P ratio is high. Conversely, the community C:P is low in the polar waters in part because the eukaryotes dominate and their C:P ratio is low. For both eukaryotes and cyanobacteria, their C:P is high in oligotrophic subtropical gyres because PO_4 is low (Figure 4c and d). This physiological effect is larger in eukaryotes than cyanobacteria because the former has greater sensitivity (i.e., larger sensitivity factor $s_{PO_4}^{P:C}$, Equation 5 , Table 2b). However, the cyanobacteria PFT's C:P ratio has an additional sensitivity to temperature (i.e., $s_T^{P:C} \neq 0$) that elevates their C:P in the lower latitudes. We do not show the C:P ratio for diazotrophs because it is very similar to that of cyanobacteria (Figure 4b, d).

In order to gain more insights into the spatial patterns of the C:P ratio (Figure 4), we examined the relationships between the C:P and C:N ratios and the four possible environmental drivers for eukaryotes and cyanobacteria (Figure 5; again, diazotrophs are not shown). The red plots show that there is a causal relationship between the ratios and the drivers as formulated by the power law model (Equations 5 and 6). The black plots show the absence of a causal relationship. For example, the C:P ratio of both eukaryotes and cyanobacteria are strongly correlated with PO_4 because there is a causal relationship (Figure 5a, b shown in red). Similarly, the C:N ratio of the same two PFTs have a strong correlation with PO_4 (Figure 5c, d in black), but there is actually not a causal relationship (i.e., $s_{PO_4}^{N:C} = 0$, Table 2b). The C:N-PO_4 correlation exists, simply because the nutrients are well correlated. Similarly, because temperature and photosynthetically active radiation

https://doi.org/10.5194/gmd-2020-408
Preprint. Discussion started: 6 January 2021

(PAR) tend to be correlated via latitude, the stoichiometry has a similar correlation to the two drivers. For example, cyanobacteria C:P has a strong correlation with both temperature and PAR (Figure 5j, 4n), but only the temperature is a real driver. Figure 5 indicates which are the dominant drivers of the C:N:P ratio in MESMO 3. For the eukaryote C:P ratio, it is PO_4. For the cyanobacteria C:P ratio, the important drivers are temperature and PO_4. For the C:N ratio for both eukaryotes and cyanobacteria, NO_3 is more important than PAR. Figure 5 also serves to remind us of one of the most basic lessons of statistics, that correlation does not indicate causation.

Figure 6 shows the community C:P and C:N ratios plotted against the four environmental drivers. Unlike Figure 5, which reflected the individual PFT's physiological response, Figure 6 includes the effect of taxonomy as well. Still, the effects of PO_4 and temperature are clearly visible on the community C:P ratio. Both low [PO_4] and warmer waters are found in the lower latitudes, so the P frugality and temperature effects are additive. The effect of NO_3 on the community C:N ratio is also very clear, but the effect of PAR is not as clear. Thus overall, the physiological effects seen in the PFT-specific C:N:P are obvious in the community C:N:P ratio.

3.2 DOM_r-enabled MESMO 3

In MESMO 2, DOC_{sl} was a standard state variable. In MESMO 3, other forms of DOM are available as options. They are the semi-labile forms of DOM: DOP_{sl}, DON_{sl}, and $DOFe_{sl}$; and the refractory forms of DOM: DOC_r, DOP_r, and DON_r. MESMO 3 is not yet calibrated with respect to all the DOM variables, but here we demonstrate their potential use in future biogeochemical investigations by presenting steady state DOM results from the model experiment *LV* (experiment ID: 201027c). In this run, all three sinks of DOM_r are activated: slow background decay, photodegradation, and degradation in hydrothermal vents.

The experiment name *LV* stands for "literature values." In *LV*, we use the literature values for the key DOM remineralization model parameters (Table 2d) and $fDOM_r = 0.01$ (Hansell, 2013). All other model parameter values in the *LV* run are identical to the standard MESMO 3 model (Table 2). The black lines in Figure 7 show the global mean vertical profiles of the total DOC ($DOC_t = DOC_{sl} + DOC_r$) in solid line and DOC_r in dashed line. Qualitatively, the simulated profiles are consistent with the observations, showing a near-uniform DOC_r concentration and a DOC_{sl} profile that rapidly with depth in the top few hundred meters (Hansell, 2013). However, the simulated values reach 130 µmol kg^{-1} in the surface, which is approximately twice the observations. More typically, the observed DOC_r is 30~40 µmol kg^{-1}, and the observed DOC_{sl} attenuates with depth from 30~40 µmol kg^{-1} near the surface. So their sum, which is represented by DOC_t, is approximately 60-80 µmol kg^{-1} at the surface in observations.

Figure 8 adds a lateral perspective to Figure 7. The rapid DOC_t attenuation in the vertical is strong in the lower latitudes where stratification is generally stronger. The transport of DOC_{sl} from the surface to deeper waters is evident in the high latitudes of the North Atlantic and the Southern Ocean. The DOC_t change in the deep ocean is limited. Observations of deep ocean DOC_t indicates a reduction by 29% or 14 µmol kg^{-1} from the deep North Atlantic to the deep North Pacific (Hansell and Carlson, 1998). Figure 8 shows that the deep ocean DOC_t gradient in *LV* is approximately 10 µmol kg^{-1} from 70-75 µmol kg^{-1} in the North Atlantic to <65 µmol kg^{-1} in the North Pacific.

The horizontal DOC_t distributions from the *LV* run can also be compared to a global extrapolation based on an artificial neural network (ANN) of the available DOC_t data (Roshan and DeVries, 2017). At the surface, the extrapolation indicates higher DOC_t concentrations in the subtropical gyres (Figure 9a), while our simulation does not clearly delineate the gyres (Figure 9c). In our model, fDOM is temperature-dependent and strongly controls the production of DOM. The surface DOC_t is thus more elevated in the lower latitudes. Interestingly, the ANN study diagnosed higher rates of DOM production in the subtropical gyres. Since the oligotrophic subtropical gyres have low NPP, the diagnosis would thus suggest that somehow fDOM is higher in the gyres. At depths, both the extrapolated and simulated DOC_t show a gradual decline in concentrations from the North Atlantic to the North Pacific (Figure 9b, d). The highest deep DOC_t in the *LV* run is seen just south of Greenland, where convection occurs in the model.

Finally, we show that the deep ocean radiocarbon aging is larger in DIC than in DOC_t in the model (Figure 10). The North Pacific-North Atlantic $\Delta^{14}C$ gradient is roughly -100‰ for DIC and -70‰ for DOC_t. The oldest DOC_t $\Delta^{14}C$ is approximately -430‰ in the North Pacific. If ^{14}C decay were the only mechanism of change along the path of the deepwater circulation, the $\Delta^{14}C$ gradient should be quite similar between DIC and DOC_t, which are both dissolved phases and transported passively by the same circulation. The one potentially important difference is that the addition of the relatively young $DI^{14}C$ and $DO^{14}C$ to the deep ocean by the "deep POC split" (see Section 2.3) impacts DOC_t $\Delta^{14}C$ more than DIC $\Delta^{14}C$, because DOC_t is two orders of magnitude lower in concentration than DIC.

In observations, the aging of DIC and DOC_t is reportedly similar in the Antarctic Bottom Water (below 4000 m) of the deep Pacific (Druffel et al., 2019). This may be explained by the fact that there would not be much deep POC split occurring so deep in the ocean. The North Pacific-North Atlantic $\Delta^{14}C$ gradient, accounting for thermonuclear bomb ^{14}C, may be as large as -100‰ for DOC_t (about -550‰ in the deep Pacific and -456‰ in the deep Atlantic) (Druffel et al., 2019). This gradient is not rigorously determined, because there is not enough data to do an objective analysis. Therefore, the equivalent $\Delta^{14}C$ gradient for DIC cannot be determined. However, the DIC $\Delta^{14}C$ endmember values by inspection (about -250‰ in the deep Pacific and -70‰ in the deep Atlantic) (Matsumoto and Key, 2004) indicate a clearly larger $\Delta^{14}C$ gradient for DIC than DOC_t as simulated by the experiment *LV*.

One lesson from the data-*LV* run mismatch in the overall DOC_t concentration (Figure 7) and surface DOC_t pattern (Figure 9) is that the parameter values from the literature do not fully capture the DOC cycle and/or MESMO 3 is still lacking some important DOC process. For example, $fDOM_r$ is a key parameter that is not well constrained by observations. Had we used 0.2% instead of 1% for $fDOM_r$, the global mean surface DOC_t drops to 76 μmol kg^{-1} (red line, Figure 7), consistent with observations. For achieving a better surface DOC_t pattern, we may need a different formulation of fDOM that is, for example, negatively related to nutrient concentrations so that fDOM increases in the oligotrophic subtropical gyres (Roshan and DeVries, 2017).

Another lesson from the DOM modeling exercise is that it is important to simulate DOP_r reasonably well in order to preserve the favorable results we achieved in MESMO 3 with respect to biological production and the phytoplankton C:N:P ratio. We find that in the experiment *LV*, the global mean DOP_r concentration becomes steady at 0.45 μmol-P kg^{-1}. Given that the mean DOC_r is about 40 μmol-C kg^{-1}, and the DOC_r:DOP_r ratio is estimated to be ~1370:1 (Letscher and Moore, 2015), DOP_r concentration should be on the order of 0.03 μmol-P kg^{-1}. Thus, the simulated DOP_r=0.45 μmol-P kg^{-1} is too high. Because there is more P in the form of DOP_r in *LV*, the oceanic inventory of PO_4 declines, causing a nearly 10% drop in export production compared to the standard MESMO 3. In *LV*, the decline in the surface ocean PO_4 that accompanies the change in the PO_4 inventory acts on the phytoplankton physiology (i.e., P effect on C:P in Equation 5), which leads to a large rise in the global mean phytoplankton community C:P export ratio from 113:1 to 127:1. The implementation of preferential remineralization of DOP (and DON) over DOC (Letscher and Moore, 2015) is one way to deal with the problem of too high DOP_r concentrations.

3.3 Large-scale patterns of N_2 fixation and denitrification

The modeled habitat of diazotrophs is concentrated in tropical and subtropical waters between 40°S and 40°N and limited by iron (Figure 1e, f). Most noticeably in North Pacific subtropical gyre, diazotrophs constitute ~40% of total NPP. The latitudinal extent of diazotrophs is mainly determined by surface nitrate availability and physical factors such as surface temperature and irradiance. Low nitrate availability in subtropical gyres gives diazotrophs a competitive advantage over small cyanobacteria. Warm temperature and high irradiance also critical physical factors that drive the growth of diazotrophs in the model.

The modeled global depth-integrated N_2 fixation is 109 Tg N yr^{-1} (Table 3), and this value falls well within the range of observational and geochemical constraints of 80 – 200 Tg N

yr^{-1} (Landolfi et al., 2018). In general, N_2 fixation occurs in the regions where the diazotroph's productivity is high, such as North Pacific and mid-to-low latitudes of the Atlantic basin (Supplementary Figure S6). The elevated N_2 fixation rate in the North Pacific, where nitrate limits eukaryotes and cyanobacteria (Figure 1b, d), can be explained by the healthy growth of diazotrophs, which is not limited by N. In the subtropical and tropical Atlantic and the Indian Ocean, high N_2 fixation is driven by elevated C:P and N:P ratio (Figure 4), exemplified by low phosphate availability and warm surface temperature. This spatial pattern agrees with a recent inverse model study (Wang et al., 2019), which showed an elevated N_2 fixation rate in subtropical gyres.

Global water-column denitrification is 109 Tg N yr^{-1} (Table 3) and is equal to the global N_2 fixation because the model has reached steady state. Denitrification is restricted to the subpolar North Pacific, where sub-surface oxygen concentration is significantly depleted (Figure S3d). Enhanced denitrification in this region is in qualitative agreement with a previous modeling study (Bianchi et al., 2018), which showed the anaerobic niche due to particle microenvironments can significantly expand the hypoxic expanses in the North Pacific. However, the extents of denitrification in our model do not include equatorial Eastern Pacific and Northern Indian Ocean, typically considered as the main hotspots for denitrification (Codispoti, 2007; Deutsch et al., 2007). This issue is typical of coarse-resolution global ocean biogeochemistry models that lack spatial resolution in reproducing intense upwelling (Marchal et al., 1998; Najjar et al., 1992; Yamanaka and Tajika, 1997).

Finally, we note that an important feature of the global ocean that is faithfully simulated in MESMO 3 is that the ratio of the global inventories of NO_3 and PO_4 is <16 at steady state (Gruber and Sarmiento, 1997). One key model parameter in achieving this result was the nitrate uptake half saturation constant of diazotrophs, $K_{NO3,3}$ in Equation 2. A large value of $K_{NO3,3}$ will make it hard for diazotrophs to obtain fixed N from NO_3, which would facilitate N_2 fixation and pushes up the global N/P ratio. With a smaller value of $K_{NO3,3}$, diazotrophs will more easily uptake NO_3, thus depressing N_2 fixation, lowering the global N/P ratio.

4. Conclusions

MESMO 3, the third and latest version of MESMO, is comprehensively described here. With a fully flexible C:N:P ratio in three PFTs, a prognostic N cycle, and more mechanistic schemes of organic matter production and remineralization, MESMO 3 reflects the evolving and accumulating knowledge of the ocean biogeochemistry. The model thus remains an effective tool for investigations of the global biogeochemical cycles especially on long time scale given the model's computational efficiency. In particular, MESMO 3 holds promise for studying the marine DOM cycle. The optional features of MESMO 3 include the semi-labile and refractory pools of C, P, N, and Fe. The fact that the literature values regarding the present marine DOM cycle are unable to simulate key observations indicates an opportunity for MESMO 3 to contribute to an improved understanding of the marine DOM cycle.

Code availability

The complete code of MESMO version 3.0 and results presented here are available at GitHub https://github.com/gaia3intc/mesmo.git and have a DOI: 10.5281/zenodo.4403605.

Author contribution

KM, TT, and JZ developed the model code. KM performed the simulations, carried out analyses, and archived the model code and results. KM and TT wrote the paper.

Acknowledgements

This work was funded by the US National Science Foundation (OCE-1827948). Numerical modeling and analysis were carried out using resources at the University of Minnesota Supercomputing Institute.

https://doi.org/10.5194/gmd-2020-408
Preprint. Discussion started: 6 January 2021

Tables

Table 1. MESMO Development

PFT = phytoplankton functional types. MESMO2 PFTs are LG = large/diatoms and SM = small. MESMO 3 PFTs are Eu = eukaryotes, Cy = cyanobacteria, and Dz = diazotrophs. OM = organic matter. RNPG = residual nitrate potential growth. T = temperature. PAR = photosynthetically active radiation. fDOM = fraction of NPP routed to dissolved organic matter (DOM). The two types of DOM are semi-labile (DOC, DOP, DON, and DOFe) and refractory (DOCr, DOPr, and DONr). Carbon isotopes (^{12}C, ^{13}C, and ^{14}C) are calculated separately for DOC and DOCr.

Table 2. MESMO 3 Biogeochemical Model Parameters Values

Table 3. Key Biogeochemical Model Diagnostics

[a]NPP for MESMO 2 was unavailable as a model output and therefore estimated from POC and fDOM=0.66. [b]The calculation of the PFT abundance requires NPP in terms of P. NPP was unavailable as a model output for MESMO 2, so PFT % was estimated from POC export.

References for independent constraints: (1) global NPP (Carr et al., 2006); (2) global POC export (DeVries and Weber, 2017); (3) global DOC export assumed to be 20% of total carbon export (Hansell et al., 2009; Roshan and DeVries, 2017); (4) global opal (Dunne et al., 2007); (5) global $CaCO_3$ export (Berelson et al., 2007); (6) global N fixation and denitrification rates (Landolfi et al., 2018); (7) uptake C:N:P ratio is based on POM measurements (Martiny et al., 2013); (8) export C:N:P ratio is assumed to equal the subsurface remineralization ratio (Anderson and Sarmiento, 1994); (9) Deep O_2 from WOA13 below 100 m (Garcia et al., 2013).

Figures

Figure 1. Schematic diagram of DOM cycling in MESMO 2 versus MESMO 3. In the new model, DOM_r can be activated. DOM_r is produced from POM breakdown, which can occur in the production layer or throughout the water column in the "deep POC split." Possible DOM_r remineralization mechanisms are the slow background degradation that occurs everywhere, thermal degradation in hydrothermal vents, and photodegradation in the surface. See text for details.

Figure 2. NPP-based surface phytoplankton functional type (PFT) abundance and nutrient limitation in MESMO 3. Fractional abundance and nutrient limitation for eukaryotes (a, b), cyanobacteria (c, d), and diazotrophs (e, f).

Figure 3. The effect of the residual nitrate potential growth (RNPG) on the eukaryote production in MESMO 3. Eukaryote NPP (a), opal export (b), and $CaCO_3$ export (c) in MESMO 3. $CaCO_3$ export in MESMO 2 (d). Unit = mol m^{-2} $year^{-1}$.

Figure 4. Uptake C:P ratio in the top 100 m in MESMO 3: (a) phytoplankton community C:P, (b) zonal mean C:P of all three PFTs and phytoplankton community, (c) eukaryote C:P, and (d) cyanobacteria C:P. The colors in (b) indicate: black = community C:P, red = eukaryote C:P, green = cyanobacteria C:P, and blue = diazotroph C:P.

Figure 5. Scatter plots of surface ocean eukaryote and cyanobacteria C:P and C:N vs. environmental drivers in MESMO 3. Columns: 1 = eukaryote C:P, 2 = cyanobacteria C:P, 3 = eukaryote C:N, and 4 = cyanobacteria C:N. Rows: 1 = PO_4, 2 = NO_3, 3 = temperature, and 4 = PAR. Red indicates causal relationship according to the power law formulation of flexible C:N:P ratio. PAR = photosynthetically active radiation in W m^{-2}.

Figure 6. Scatter plots of surface ocean community C:P and C:N vs environmental drivers in MESMO 3.

Figure 7. Global mean vertical profiles of DOC from the DOM_R-enabled MESMO 3. DOC_t (black line) and DOC_r (black dashed line) from the *LV* run. Red line is DOC_t after reducing $fDOM_r$ from 1% in *LV* to 0.2%. Unit = µmol kg^{-1}.

Figure 8. Global depth-latitude transect of DOC_t from the DOM_R-enabled MESMO 3 *LV* run. Transects are N-S along 25°W in the Atlantic, E-W along 60°S in the Southern Ocean, and N-S along 165°E in the Pacific. Unit = µmol kg^{-1}.

Figure 9. Assessment of surface and deep ocean DOC_t from the DOM_R-enabled MESMO 3 *LV* run. Data-derived DOC_t distributions in the top 100 m (a) and 2500-4000 m (b). Model-simulated DOC_t distributions in the top 100 m (c) and 2500-4000 m (d). Date-derived DOC_t are from Roshan and DeVries (Roshan and DeVries, 2017). Unit = µmol kg^{-1}.

Figure 10. $\Delta^{14}C$ of deep ocean DIC (a) and DOC_t (b) from the DOM_R-enabled MESMO 3 *LV* run. Vertical average over 2500-4000 m water depth. Unit = ‰.

References:

Anderson, L. A. and Sarmiento, J. L.: Redfield ratios of remineralization determined by nutrient data analysis, Global Biogeochem. Cycles, 8(1), 65–80, doi:10.1029/93GB03318, 1994.

Archer, D., Eby, M., Brovkin, V., Ridgwell, A., Cao, L., Mikolajewicz, U., Caldeira, K., Matsumoto, K., Munhoven, G., Montenegro, A. and Tokos, K.: Atmospheric Lifetime of Fossil Fuel Carbon Dioxide, Annu. Rev. Earth Planet. Sci., 37(1), 117–134, doi:10.1146/annurev.earth.031208.100206, 2009.

Arteaga, L., Pahlow, M. and Oschlies, A.: Global patterns of phytoplankton nutrient and light colimitation inferred from an optimality-based model, Global Biogeochem. Cycles, 28(7), 648–661, doi:10.1002/2013GB004668, 2014.

Balch, W. M., Bates, N. R., Lam, P. J., Twining, B. S., Rosengard, S. Z., Bowler, B. C., Drapeau, D. T., Garley, R., Lubelczyk, L. C., Mitchell, C. and Rauschenberg, S.: Factors regulating the Great Calcite Belt in the Southern Ocean and its biogeochemical significance, Global Biogeochem. Cycles, 30(8), 1124–1144, doi:10.1002/2016GB005414, 2016.

Berelson, W. M., Balch, W. M., Najjar, R., Feely, R. A., Sabine, C. and Lee, K.: Relating estimates of CaCO3 production, export, and dissolution in the water column to measurements of CaCO3 rain into sediment traps and dissolution on the sea floor:A revised global carbonate budget, Global Biogeochem. Cycles, 21(1), 1–15, doi:10.1029/2006GB002803, 2007.

Bianchi, D., Weber, T. S., Kiko, R. and Deutsch, C.: Global niche of marine anaerobic metabolisms expanded by particle microenvironments, Nat. Geosci., 11(4), 263–268, doi:10.1038/s41561-018-0081-0, 2018.

Brzezinski, M. A.: A switch from Si(OH) 4 to NO 3 – depletion in the glacial Southern Ocean, Geophys. Res. Lett., 29(12), doi:10.1029/2001gl014349, 2002.

Cao, L., Eby, M., Ridgwell, A., Caldeira, K., Archer, D., Ishida, A., Joos, F., Matsumoto, K., Mikolajewicz, U., Mouchet, A., Orr, J. C., Plattner, G.-K., Schlitzer, R., Tokos, K., Totterdell, I., Tschumi, T., Yamanaka, Y. and Yool, A.: The role of ocean transport in the uptake of anthropogenic CO_2, Biogeosciences, 6(3), 375–390, doi:10.5194/bg-6-375-2009, 2009.

Carr, M. E., Friedrichs, M. A. M., Schmeltz, M., Noguchi Aita, M., Antoine, D., Arrigo, K. R., Asanuma, I., Aumont, O., Barber, R., Behrenfeld, M., Bidigare, R., Buitenhuis, E. T., Campbell, J., Ciotti, A., Dierssen, H., Dowell, M., Dunne, J., Esaias, W., Gentili, B., Gregg, W., Groom, S., Hoepffner, N., Ishizaka, J., Kameda, T., Le Quéré, C., Lohrenz, S., Marra, J., Mélin, F., Moore, K., Morel, A., Reddy, T. E., Ryan, J., Scardi, M., Smyth, T., Turpie, K., Tilstone, G., Waters, K. and Yamanaka, Y.: A comparison of global estimates of marine primary production from ocean color, Deep. Res. Part II Top. Stud. Oceanogr., 53(5–7), 741–770, doi:10.1016/j.dsr2.2006.01.028, 2006.

Cheng, H., Edwards, R. L., Southon, J., Matsumoto, K., Feinberg, J. M., Sinha, A., Zhou, W., Li, H., Li, X., Xu, Y., Chen, S., Tan, M., Wang, Q., Wang, Y., Ning, Y., Lawrence Edwards, R., Southon, J., Matsumoto, K., Feinberg, J. M., Sinha, A., Zhou, W., Li, H., Li, X., Xu, Y., Chen, S., Tan, M., Wang, Q., Wang, Y. and Ning, Y.: Atmospheric 14C/12C changes during the last glacial period from hulu cave, Science (80-.)., 362(6420), 1293–1297, doi:10.1126/science.aau0747, 2018.

Chien, C. Te, Pahlow, M., Schartau, M. and Oschlies, A.: Optimality-based non-Redfield plankton-ecosystem model (OPEM v1.1) in UVic-ESCM 2.9 - Part 2: Sensitivity analysis and model calibration, Geosci. Model Dev., 13(10), 4691–4712, doi:10.5194/gmd-13-4691-2020, 2020.

Claussen, M., Mysak, L., Weaver, A., Crucifix, M., Fichefet, T., Loutre, M. F., Weber, S., Alcamo, J., Alexeev, V., Berger, A., Calov, R., Ganopolski, A., Goosse, H., Lohmann, G., Lunkeit, F., Mokhov, I., Petoukhov, V., Stone, P. and Wang, Z.: Earth system models of intermediate complexity: Closing the gap in the spectrum of climate system models, Clim. Dyn., 18(7), 579–586, doi:10.1007/s00382-001-0200-1, 2002.

Codispoti, L. A.: An oceanic fixed nitrogen sink exceeding 400 Tg N a-1 vs the concept of homeostasis in the fixed-nitrogen inventory, Biogeosciences, 4(2), 233–253, doi:10.5194/bg-4-233-2007, 2007.

Deutsch, C., Sarmiento, J. L., Sigman, D. M., Gruber, N. and Dunne, J. P.: Spatial coupling of nitrogen inputs and losses in the ocean, Nature, 445(7124), 163–167, doi:10.1038/nature05392, 2007.

DeVries, T. and Weber, T.: The export and fate of organic matter in the ocean: New constraints from combining satellite and oceanographic tracer observations, Global Biogeochem. Cycles, 31(3), 535–555, doi:10.1002/2016GB005551, 2017.

Druffel, E. R. M., Williams, P. M., Bauer, J. E. and Ertel, J. R.: Cycling of dissolved and particulate organic matter in the open ocean, J. Geophys. Res., 97(C10), 15639, doi:10.1029/92JC01511, 1992.

Druffel, E. R. M., Griffin, S., Wang, N., Garcia, N. G., McNichol, A. P., Key, R. M. and Walker, B. D.: Dissolved Organic Radiocarbon in the Central Pacific Ocean, Geophys. Res. Lett., 46(10), 5396–5403, doi:10.1029/2019GL083149, 2019.

Dunne, J. P., Armstrong, R. A., Gnanadesikan, A. and Sarmiento, J. L.: Empirical and mechanistic models for the particle export ratio, Global Biogeochem. Cycles, 19(4), n/a-n/a, doi:10.1029/2004GB002390, 2005.

Dunne, J. P., Sarmiento, J. L. and Gnanadesikan, A.: A synthesis of global particle export from the surface ocean and cycling through the ocean interior and on the seafloor, Global Biogeochem. Cycles, 21(4), doi:10.1029/2006GB002907, 2007.

Eby, M., Weaver, A. J., Alexander, K., Zickfeld, K., Abe-Ouchi, A., Cimatoribus, A. A., Crespin, E., Drijfhout, S. S., Edwards, N. R., Eliseev, A. V., Feulner, G., Fichefet, T., Forest, C. E., Goosse, H., Holden, P. B., Joos, F., Kawamiya, M., Kicklighter, D., Kienert, H., Matsumoto, K., Mokhov, I. I., Monier, E., Olsen, S. M., Pedersen, J. O. P., Perrette, M., Philippon-Berthier, G., Ridgwell, A., Schlosser, A., Schneider von Deimling, T., Shaffer, G., Smith, R. S., Spahni, R., Sokolov, A. P., Steinacher, M., Tachiiri, K., Tokos, K., Yoshimori, M., Zeng, N. and Zhao, F.: Historical and idealized climate model experiments: an intercomparison of Earth system models of intermediate complexity, Clim. Past, 9(3), 1111–1140, doi:10.5194/cp-9-1111-2013, 2013.

Edwards, N. R. and Marsh, R.: Uncertainties due to transport-parameter sensitivity in an efficient 3-D ocean-climate model, Clim. Dyn., 24(4), 415–433, doi:10.1007/s00382-004-0508-8, 2005.

Eppley, R. W.: Temperature and phytoplankton growth in the sea, Fish. Bull., 70(4), 1063–85, 1972.

Galbraith, E. D. and Martiny, A. C.: A simple nutrient-dependence mechanism for predicting the stoichiometry of marine ecosystems, Proc. Natl. Acad. Sci., 112(27), 8199–8204, doi:10.1073/pnas.1423917112, 2015.

Garcia, H. E., Boyer, T. P., Locarnini, R. A., Antonov, J. I., Mishonov, A. V., Baranova, O. K., Zweng, M. M., Reagan, J. R. and Johnson, D. R.: World Ocean Atlas 2013. Volume 3:

Dissolved oxygen, apparent oxygen utilization, and oxygen saturation, edited by S. Levitus and A. Mishonov., 2013.

Gruber, N. and Sarmiento, J. L.: Global patterns of marine nitrogen fixation and denitrification, Global Biogeochem. Cycles, 11(2), 235–266, doi:10.1029/97GB00077, 1997.

Hansell, D. A.: Recalcitrant Dissolved Organic Carbon Fractions, Ann. Rev. Mar. Sci., 5(1), 421–445, doi:10.1146/annurev-marine-120710-100757, 2013.

Hansell, D. A. and Carlson, C. A.: Deep-ocean gradients in the concentration of dissolved organic carbon, Nature, 395(6699), 263–266, doi:10.1038/26200, 1998.

Hansell, D. A., Carlson, C. A., Repeta, D. J. and Schlitzer, R.: Dissolved Organic Matter in the Ocean: A Controversy stimulates new insights, Oceanography, 22(4), 202–211, doi:https://doi.org/10.5670/oceanog.2009.109, 2009.

Henson, S. A., Sanders, R., Madsen, E., Morris, P. J., Le Moigne, F. and Quartly, G. D.: A reduced estimate of the strength of the ocean's biological carbon pump, Geophys. Res. Lett., 38(4), n/a-n/a, doi:10.1029/2011GL046735, 2011.

Hutchins, D. A. and Bruland, K. W.: Iron-limited growth and Si:N ratios in a costal upwelling regime, Nature, 393(June), 561–564, 1998.

Joos, F., Roth, R., Fuglestvedt, J. S., Peters, G. P., Enting, I. G., Von Bloh, W., Brovkin, V., Burke, E. J., Eby, M., Edwards, N. R., Friedrich, T., Frölicher, T. L., Halloran, P. R., Holden, P. B., Jones, C., Kleinen, T., Mackenzie, F. T., Matsumoto, K., Meinshausen, M., Plattner, G. K., Reisinger, A., Segschneider, J., Shaffer, G., Steinacher, M., Strassmann, K., Tanaka, K., Timmermann, A. and Weaver, A. J.: Carbon dioxide and climate impulse response functions for the computation of greenhouse gas metrics: A multi-model analysis, Atmos. Chem. Phys., 13(5), 2793–2825, doi:10.5194/acp-13-2793-2013, 2013.

Kwiatkowski, L., Aumont, O., Bopp, L. and Ciais, P.: The Impact of Variable Phytoplankton Stoichiometry on Projections of Primary Production, Food Quality, and Carbon Uptake in the Global Ocean, Global Biogeochem. Cycles, 32(4), 516–528, doi:10.1002/2017GB005799, 2018.

Kwiatkowski, L., Aumont, O. and Bopp, L.: Consistent trophic amplification of marine biomass declines under climate change, Glob. Chang. Biol., 25(1), 218–229, doi:10.1111/gcb.14468, 2019.

Landolfi, A., Kähler, P., Koeve, W. and Oschlies, A.: Global marine N2 fixation estimates: From observations to models, Front. Microbiol., 9(SEP), 1–8, doi:10.3389/fmicb.2018.02112, 2018.

Lang, S. Q., Butterfield, D. A., Lilley, M. D., Paul Johnson, H. and Hedges, J. I.: Dissolved organic carbon in ridge-axis and ridge-flank hydrothermal systems, Geochim. Cosmochim. Acta, 70(15), 3830–3842, doi:10.1016/j.gca.2006.04.031, 2006.

Laufkötter, C., John, J. G., Stock, C. A. and Dunne, J. P.: Temperature and oxygen dependence of the remineralization of organic matter, Global Biogeochem. Cycles, 31(7), 1038–1050, doi:10.1002/2017GB005643, 2017.

Laws, E. A., Falkowski, P. G., Smith, W. O., Ducklow, H. W. and McCarthy, J. J.: Temperature effects on export production in the open ocean, Global Biogeochem. Cycles, 14(4), 1231–1246, doi:10.1029/1999GB001229, 2000.

Lee, S. Y., Chiang, J. C. H., Matsumoto, K. and Tokos, K. S.: Southern Ocean wind response to North Atlantic cooling and the rise in atmospheric CO 2 : Modeling perspective and paleoceanographic implications, Paleoceanography, 26, 1–16, doi:10.1029/2010PA002004, 2011.

Lenton, T. M., Williamson, M. S., Edwards, N. R., Marsh, R., Price, A. R., Ridgwell, A. J., Shepherd, J. G. and Cox, S. J.: Millennial timescale carbon cycle and climate change in an efficient Earth system model, Clim. Dyn., 26(7–8), 687–711, doi:10.1007/s00382-006-0109-9, 2006.

Letscher, R. T. and Moore, J. K.: Preferential remineralization of dissolved organic phosphorus and non-Redfield DOM dynamics in the global ocean: Impacts on marine productivity, nitrogen fixation, and carbon export, Global Biogeochem. Cycles, 29(3), 325–340, doi:10.1002/2014GB004904, 2015.

Levitus, S.: Climatological atlas of the world ocean, US Department of Commerce, National Oceanic and Atmospheric Administration., 1982.

Mahowald, N. M., Muhs, D. R., Levis, S., Rasch, P. J., Yoshioka, M., Zender, C. S. and Luo, C.: Change in atmospheric mineral aerosols in response to climate: Last glacial period, preindustrial, modern, and doubled carbon dioxide climates, J. Geophys. Res. Atmos., 111(D10), n/a-n/a, doi:10.1029/2005JD006653, 2006.

Marchal, O., Stocker, T. F. and Joos, F.: A latitude-depth, circulation-biogeochemical ocean model for palaeoclimate studies. Development and sensitivities, Tellus, Ser. B Chem. Phys. Meteorol., 50B(3), 290–316, doi:10.1034/j.1600-0889.1998.t01-2-00006.x, 1998.

Martiny, A. C., Pham, C. T. A., Primeau, F. W., Vrugt, J. A., Moore, J. K., Levin, S. A. and Lomas, M. W.: Strong latitudinal patterns in the elemental ratios of marine plankton and organic matter, Nat. Geosci., 6(4), 279–283, doi:10.1038/ngeo1757, 2013.

Mather, R. L., Reynolds, S. E., Wolff, G. A., Williams, R. G., Torres-Valdes, S., Woodward, E. M. S., Landolfi, A., Pan, X., Sanders, R. and Achterberg, E. P.: Phosphorus cycling in the North and South Atlantic Ocean subtropical gyres, Nat. Geosci., 1(7), 439–443, doi:10.1038/ngeo232, 2008.

Matsumoto, K. and Key, R. M.: Natural radiocarbon distribution in the deep ocean, in Global Environmental Change in the Ocean and on Land, edited by M. Shiyomi, H. Kawahata, H. Koizumi, A. Tsuda, and Y. Awaya, pp. 45–58, Terrapub, Tokyo., 2004.

Matsumoto, K. and McNeil, B.: Decoupled response of ocean acidification to variations in climate sensitivity, J. Clim., 26, 1764–1771, doi:10.1175/JCLI-D-12-00290.1, 2012.

Matsumoto, K. and Tanioka, T.: Shifts in regional production as a driver of future global ocean production stoichiometry, Environ. Res. Lett., doi:10.1088/1748-9326/abc4b0, 2020.

Matsumoto, K. and Yokoyama, Y.: Atmospheric Δ 14 C reduction in simulations of Atlantic overturning circulation shutdown, Global Biogeochem. Cycles, 27(2), 296–304, doi:10.1002/gbc.20035, 2013.

Matsumoto, K., Tokos, K., Price, A. R. and Cox, S. J.: First description of the Minnesota Earth System Model for Ocean biogeochemistry (MESMO 1.0), Geosci. Model Dev., 1(1), 1–15, doi:10.5194/gmd-1-1-2008, 2008.

Matsumoto, K., Tokos, K., Chikamoto, M. and Ridgwell, A.: Characterizing post-industrial changes in the ocean carbon cycle in an Earth system model, Tellus B Chem. Phys. Meteorol., 62(4), 296–313, doi:10.1111/j.1600-0889.2010.00461.x, 2010.

Matsumoto, K., Tokos, K., Huston, A. and Joy-Warren, H.: MESMO 2: a mechanistic marine silica cycle and coupling to a simple terrestrial scheme, Geosci. Model Dev., 6(2), 477–494, doi:10.5194/gmd-6-477-2013, 2013.

Matsumoto, K., Rickaby, R. and Tanioka, T.: Carbon Export Buffering and CO2 Drawdown by

Flexible Phytoplankton C:N:P Under Glacial Conditions, Paleoceanogr. Paleoclimatology, 35(7), 1–22, doi:10.1029/2019PA003823, 2020.

Moore, J. K., Doney, S. C. and Lindsay, K.: Upper ocean ecosystem dynamics and iron cycling in a global three-dimensional model, Global Biogeochem. Cycles, 18(4), 1–21, doi:10.1029/2004GB002220, 2004.

Mopper, K., Zhou, X., Kieber, R. J., Kieber, D. J., Sikorski, R. J. and Jones, R. D.: Photochemical degradation of dissolved organic carbon and its impact on the oceanic carbon cycle, Nature, 353(6339), 60–62, doi:10.1038/353060a0, 1991.

Najjar, R. G., Sarmiento, J. L. and Toggweiler, J. R.: Downward transport and fate of organic matter in the ocean: Simulations with a general circulation model, Global Biogeochem. Cycles, 6(1), 45–76, doi:10.1029/91GB02718, 1992.

Pahlow, M. and Oschlies, A.: Chain model of phytoplankton P, N and light colimitation, Mar. Ecol. Prog. Ser., 376, 69–83, doi:10.3354/meps07748, 2009.

Pahlow, M. and Oschlies, A.: Optimal allocation backs droop's cell-quota model, Mar. Ecol. Prog. Ser., 473(2010), 1–5, doi:10.3354/meps10181, 2013.

Pahlow, M., Dietze, H. and Oschlies, A.: Optimality-based model of phytoplankton growth and diazotrophy, Mar. Ecol. Prog. Ser., 489, 1–16, doi:10.3354/meps10449, 2013.

Pahlow, M., Chien, C. Te, Arteaga, L. A. and Oschlies, A.: Optimality-based non-Redfield plankton-ecosystem model (OPEM v1.1) in UVic-ESCM 2.9 - Part 1: Implementation and model behaviour, Geosci. Model Dev., 13(10), 4663–4690, doi:10.5194/gmd-13-4663-2020, 2020.

Paulsen, H., Ilyina, T., Six, K. D. and Stemmler, I.: Incorporating a prognostic representation of marine nitrogen fixers into the global ocean biogeochemical model HAMOCC, J. Adv. Model. Earth Syst., 9(1), 438–464, doi:10.1002/2016MS000737, 2017.

Ridgwell, A.: Glacial-interglacial perturbations in the global carbon cycle, Ph, D. thesis, 134 pp., Univ. East Anglia, Norwich, U. K. Ridgwell, A. J., U. Edwards, 2001.

Ridgwell, A., Hargreaves, J. C., Edwards, N. R., Annan, J. D., Lenton, T. M., Marsh, R., Yool, A. and Watson, A.: Marine geochemical data assimilation in an efficient Earth System Model of global biogeochemical cycling, Biogeosciences, 4(4), 87–104, doi:10.5194/bg-4-87-2007, 2007.

Ridgwell, A. J., Watson, A. J. and Archer, D. E.: Modeling the response of the oceanic Si inventory to perturbation, and consequences for atmospheric CO $_2$, Global Biogeochem. Cycles, 16(4), 19-1-19–25, doi:10.1029/2002GB001877, 2002.

Roshan, S. and DeVries, T.: Efficient dissolved organic carbon production and export in the oligotrophic ocean, Nat. Commun., 8(1), 2036, doi:10.1038/s41467-017-02227-3, 2017.

Sarmiento, J. L., Gruber, N., Brzezinski, M. A. and Dunne, J. P.: High-latitude controls of thermocline nutrients and low latitude biological productivity, Nature, 427(6969), 56–60, doi:10.1038/nature02127, 2004.

Sun, X. and Matsumoto, K.: Effects of sea ice on atmospheric p CO 2 : A revised view and implications for glacial and future climates, J. Geophys. Res., 115(G02015), doi:10.1029/2009JG001023, 2010.

Sunda, W. and Huntsman, S.: Iron uptake and growth limitation in oceanic and coastal phytoplankton, Mar. Chem., 50(1–4), 189–206, doi:10.1016/0304-4203(95)00035-P, 1995.

Sverdrup, H. U.: On the conditions for the vernal blooming of phytoplankton, J. Cons. Perm. Int. Pour l'Exploration La Mer, 18, 287–195, 1953.

Takeda, S.: Influence of iron availability on nutrient consumption ratio, Nature, 393(JUNE), 774–777, 1998.

Tanioka, T. and Matsumoto, K.: Buffering of Ocean Export Production by Flexible Elemental Stoichiometry of Particulate Organic Matter, Global Biogeochem. Cycles, 31(10), 1528–1542, doi:10.1002/2017GB005670, 2017.

Tanioka, T. and Matsumoto, K.: A meta-analysis on environmental drivers of marine phytoplankton C : N : P, Biogeosciences, 17(11), 2939–2954, doi:10.5194/bg-17-2939-2020, 2020a.

Tanioka, T. and Matsumoto, K.: Stability of Marine Organic Matter Respiration Stoichiometry, Geophys. Res. Lett., 47(1), 1–10, doi:10.1029/2019GL085564, 2020b.

Ushie, H. and Matsumoto, K.: The role of shelf nutrients on glacial-interglacial CO 2 : A negative feedback, Global Biogeochem. Cycles, 26, 1–10, doi:10.1029/2011GB004147, 2012.

Wang, W.-L., Moore, J. K., Martiny, A. C. and Primeau, F. W.: Convergent estimates of marine nitrogen fixation, Nature, 566(7743), 205–211, doi:10.1038/s41586-019-0911-2, 2019.

Wanninkhof, R.: Relationship between wind speed and gas exchange over the ocean, J. Geophys. Res., 97(C5), 7373–7382, doi:10.1029/92JC00188, 1992.

Weaver, A. J., Sedlá, J., Eby, M., Alexander, K., Crespin, E., Fichefet, T., Philippon-berthier, G., Joos, F., Kawamiya, M., Matsumoto, K., Steinacher, M., Tachiiri, K., Tokos, K., Yoshimori, M. and Zickfeld, K.: Stability of the Atlantic meridional overturning circulation : A model intercomparison, Geophys. Res. Lett., 39, 1–7, doi:10.1029/2012GL053763, 2012.

Yamanaka, Y. and Tajika, E.: Role of dissolved organic matter in the marine biogeochemical cycle: Studies using an ocean biogeochemical general circulation model, Global Biogeochem. Cycles, 11(4), 599–612, doi:10.1029/97GB02301, 1997.

Yamanaka, Y., Yoshie, N., Fujii, M., Aita, M. N. and Kishi, M. J.: An Ecosystem Model Coupled with Nitrogen-Silicon-Carbon Cycles Applied to Station A7 in the Northwestern Pacific, J. Oceanogr., 60(2), 227–241, doi:10.1023/B:JOCE.0000038329.91976.7d, 2004.

Zickfeld, K., Eby, M., Weaver, A. J., Alexander, K., Crespin, E., Edwards, N. R., Eliseev, A. V., Feulner, G., Fichefet, T., Forest, C. E., Friedlingstein, P., Goosse, H., Holden, P. B., Joos, F., Kawamiya, M., Kicklighter, D., Kienert, H., Matsumoto, K., Mokhov, I. I., Monier, E., Olsen, S. M., Pedersen, J. O. P., Perrette, M., Philippon-Berthier, G., Ridgwell, A., Schlosser, A., Von Deimling, T. S., Shaffer, G., Sokolov, A., Spahni, R., Steinacher, M., Tachiiri, K., Tokos, K. S., Yoshimori, M., Zeng, N. and Zhao, F.: Long-Term climate change commitment and reversibility: An EMIC intercomparison, J. Clim., 26(16), 5782–5809, doi:10.1175/JCLI-D-12-00584.1, 2013.

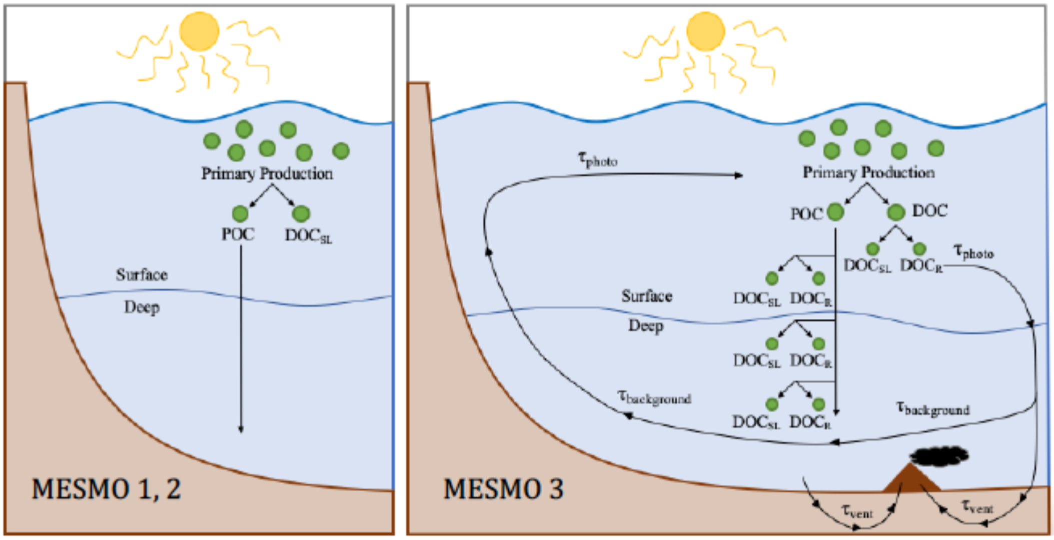

Figure 1. Schematic diagram of DOM cycling in MESMO 2 versus MESMO 3. In the new model, $\mathrm{DOM_r}$ can be activated. $\mathrm{DOM_r}$ is produced from POM breakdown, which can occur in the production layer or throughout the water column in the "deep POC split." Possible $\mathrm{DOM_r}$ remineralization mechanisms are the slow background degradation that occurs everywhere, thermal degradation in hydrothermal vents, and photodegradation in the surface. See text for details.

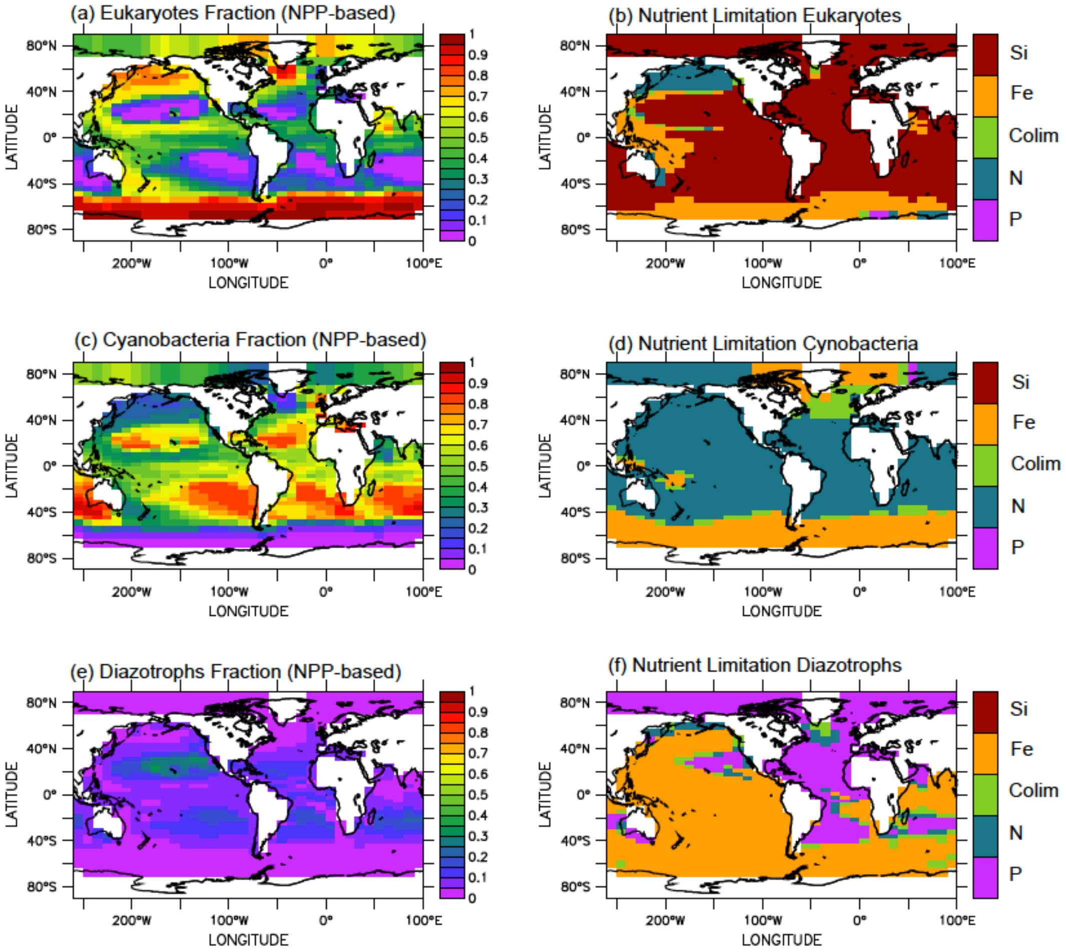

Figure 2. NPP-based surface phytoplankton functional type (PFT) abundance and nutrient limitation in MESMO 3. Fractional abundance and nutrient limitation for eukaryotes (a, b), cyanobacteria (c, d), and diazotrophs (e, f).

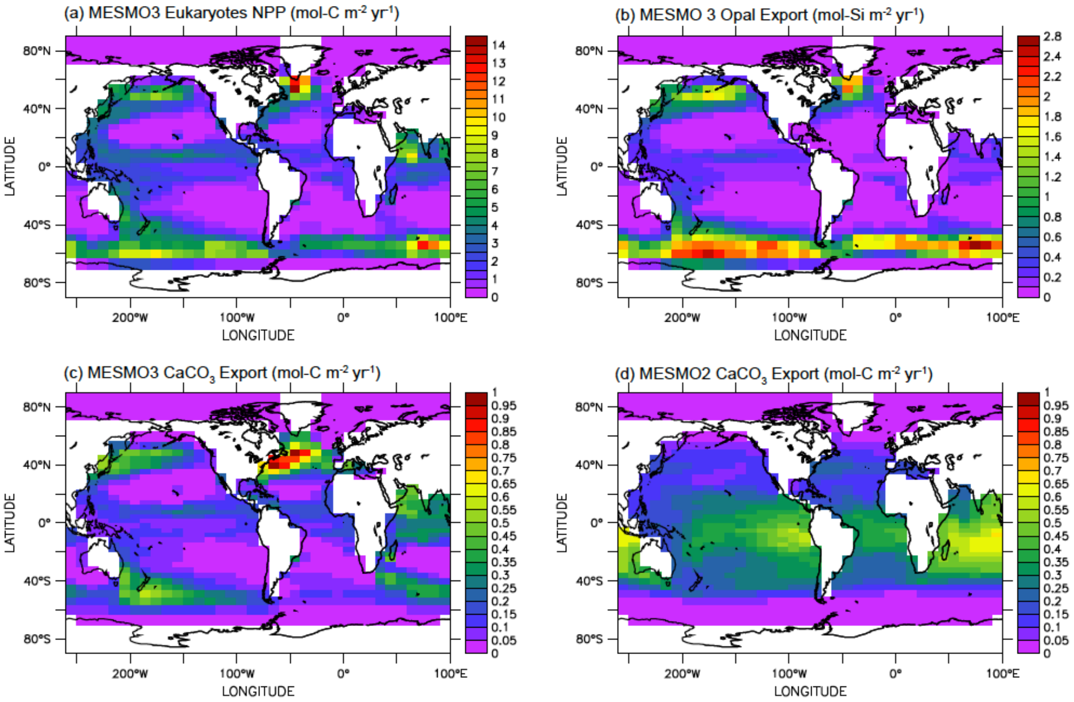

Figure 3. The effect of the residual nitrate potential growth (RNPG) on the eukaryote production in MESMO 3. Eukaryote NPP (a), opal export (b), and $CaCO_3$ export (c) in MESMO 3. $CaCO_3$ export in MESMO 2 (d). Unit = mol m^{-2} $year^{-1}$.

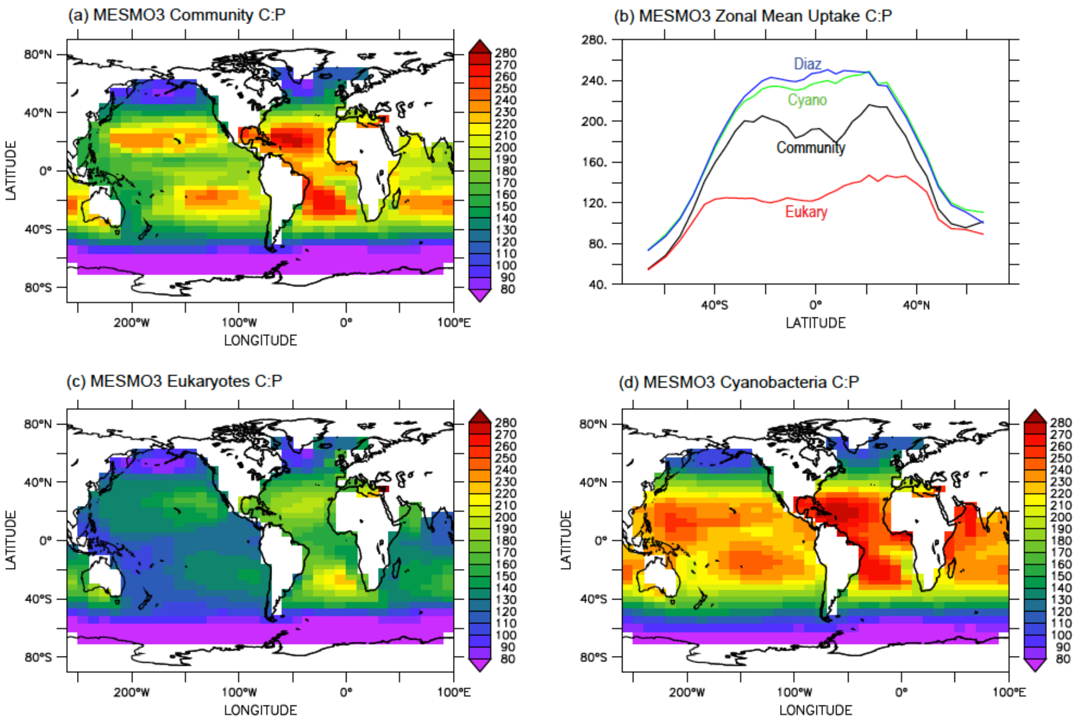

Figure 4. Uptake C:P ratio in the top 100 m in MESMO 3: (a) phytoplankton community C:P, (b) zonal mean C:P of all three PFTs and phytoplankton community, (c) eukaryote C:P, and (d) cyanobacteria C:P. The colors in (b) indicate: black = community C:P, red = eukaryote C:P, green = cyanobacteria C:P, and blue = diazotroph C:P.

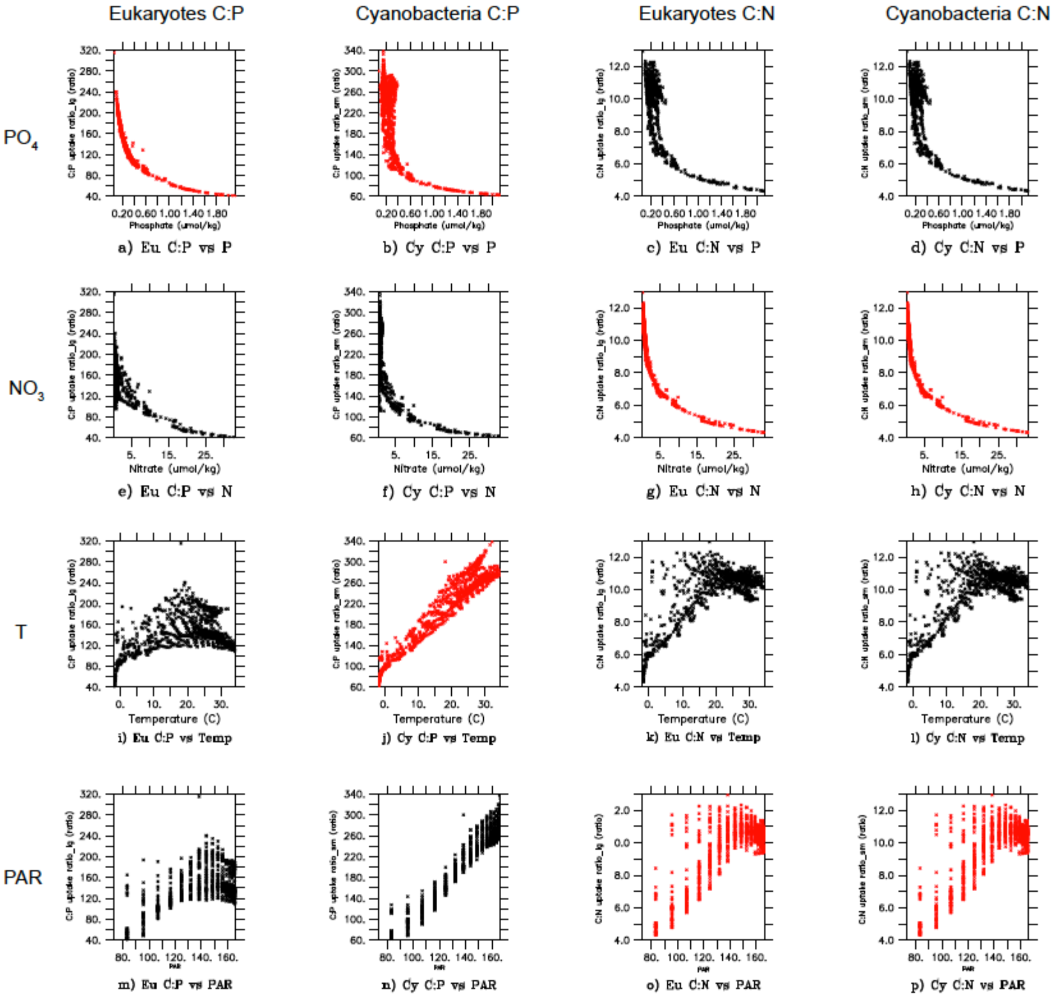

a) Eu C:P vs P
b) Cy C:P vs P
c) Eu C:N vs P
d) Cy C:N vs P
e) Eu C:P vs N
f) Cy C:P vs N
g) Eu C:N vs N
h) Cy C:N vs N
i) Eu C:P vs Temp
j) Cy C:P vs Temp
k) Eu C:N vs Temp
l) Cy C:N vs Temp
m) Eu C:P vs PAR
n) Cy C:P vs PAR
o) Eu C:N vs PAR
p) Cy C:N vs PAR

Figure 5. Scatter plots of surface ocean eukaryote and cyanobacteria C:P and C:N vs. environmental drivers in MESMO 3. Columns: 1 = eukaryote C:P, 2 = cyanobacteria C:P, 3 = eukaryote C:N, and 4 = cyanobacteria C:N. Rows: 1 = PO_4, 2 = NO_3, 3 = temperature, and 4 = PAR. Red indicates causal relationship according to the power law formulation of flexible C:N:P ratio. PAR = photosynthetically active radiation in W m^{-2}.

https://doi.org/10.5194/gmd-2020-408
Preprint. Discussion started: 6 January 2021

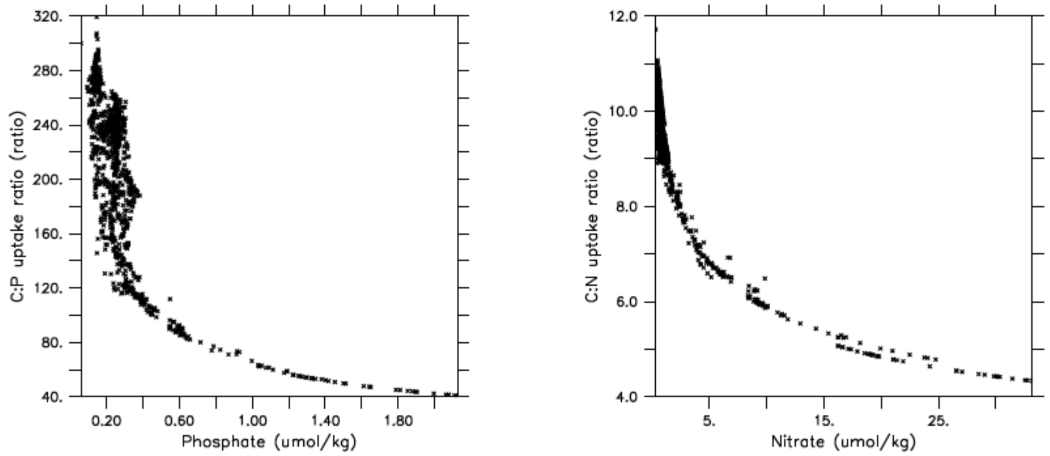

com C:P vs P

com C:N vs N

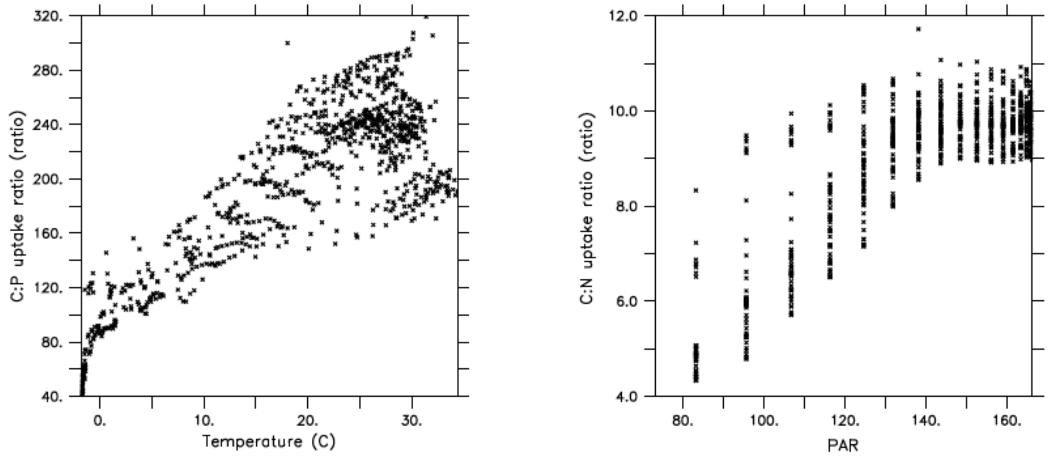

com C:P vs Temp

com C:N vs PAR

Figure 6. Scatter plots of surface ocean community C:P and C:N vs environmental drivers in MESMO 3.

https://doi.org/10.5194/gmd-2020-408
Preprint. Discussion started: 6 January 2021

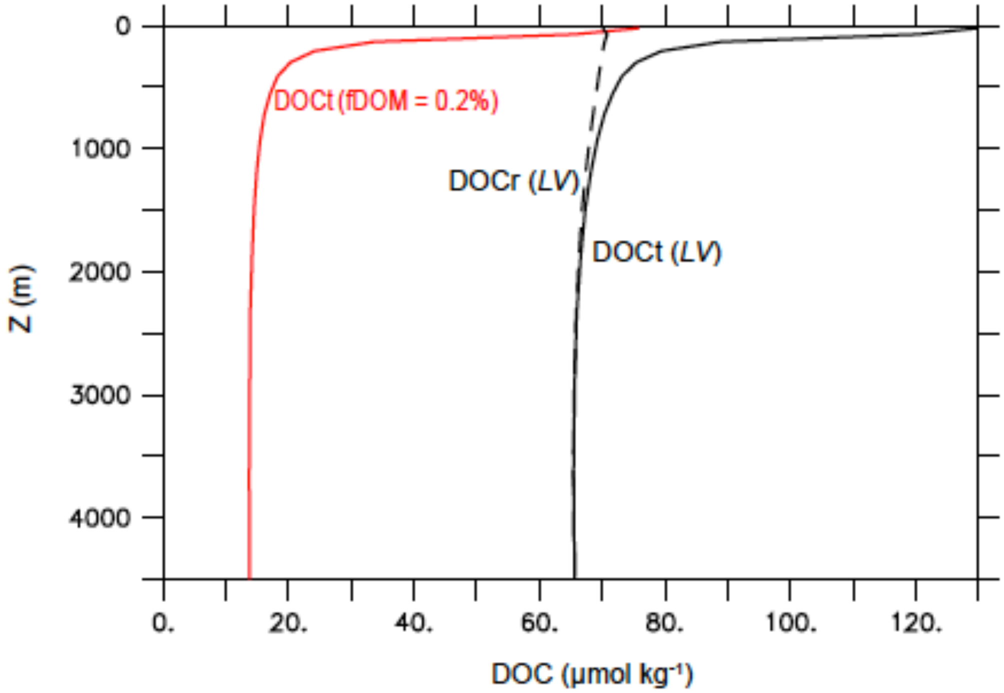

Figure 7. Global mean vertical profiles of DOC from the DOM_R-enabled MESMO 3. DOC_t (black line) and DOC_r (black dashed line) from the *LV* run. Red line is DOC_t after reducing $fDOM_r$ from 1% in *LV* to 0.2%. Unit = µmol kg^{-1}.

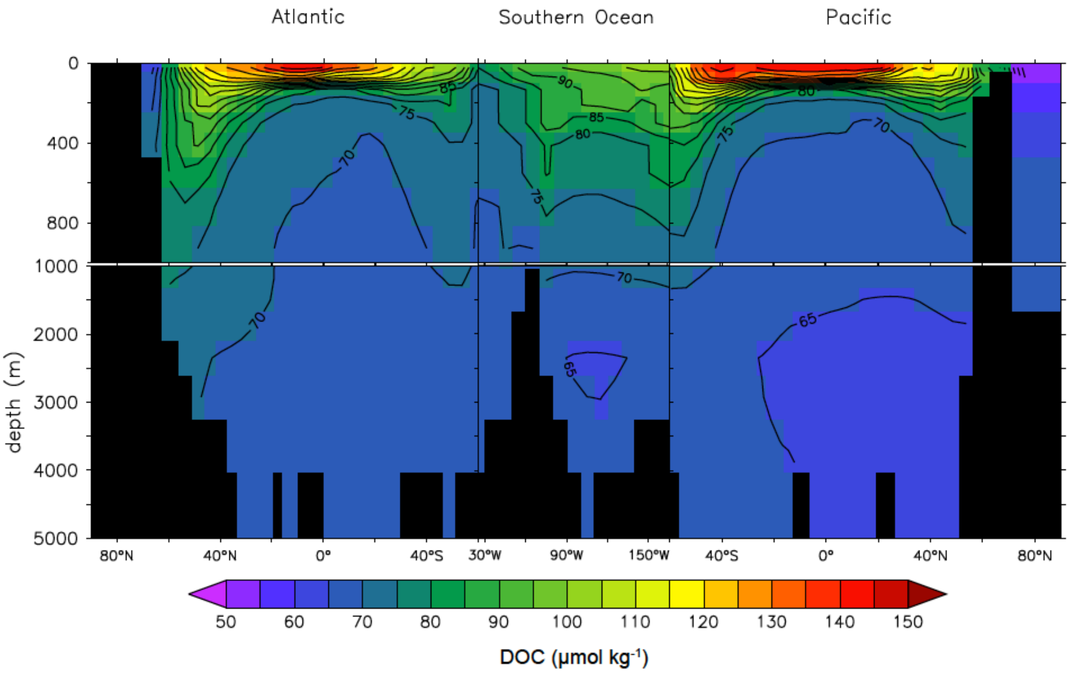

Figure 8. Global depth-latitude transect of DOC_t from the DOM_R-enabled MESMO 3 *LV* run. Transects are N-S along 25°W in the Atlantic, E-W along 60°S in the Southern Ocean, and N-S along 165°E in the Pacific. Unit = μmol kg^{-1}.

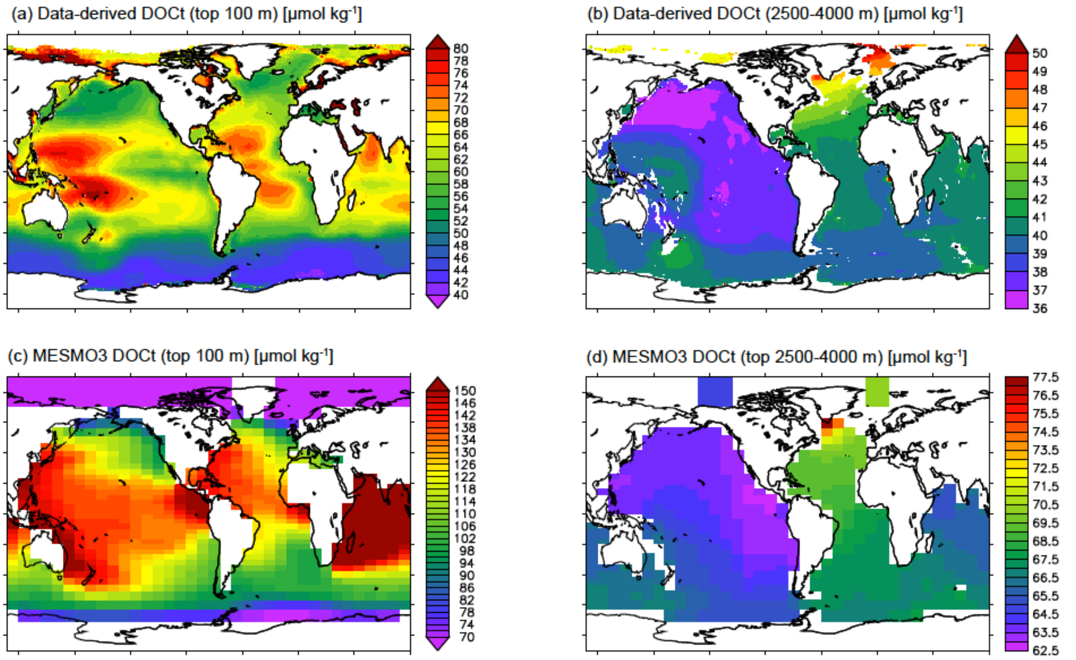

Figure 9. Assessment of surface and deep ocean DOC$_t$ from the DOM$_R$-enabled MESMO 3 *LV* run. Data-derived DOC$_t$ distributions in the top 100 m (a) and 2500-4000 m (b). Model-simulated DOC$_t$ distributions in the top 100 m (c) and 2500-4000 m (d). Date-derived DOC$_t$ are from Roshan and DeVries (Roshan and DeVries, 2017). Unit = μmol kg^{-1}.

https://doi.org/10.5194/gmd-2020-408
Preprint. Discussion started: 6 January 2021

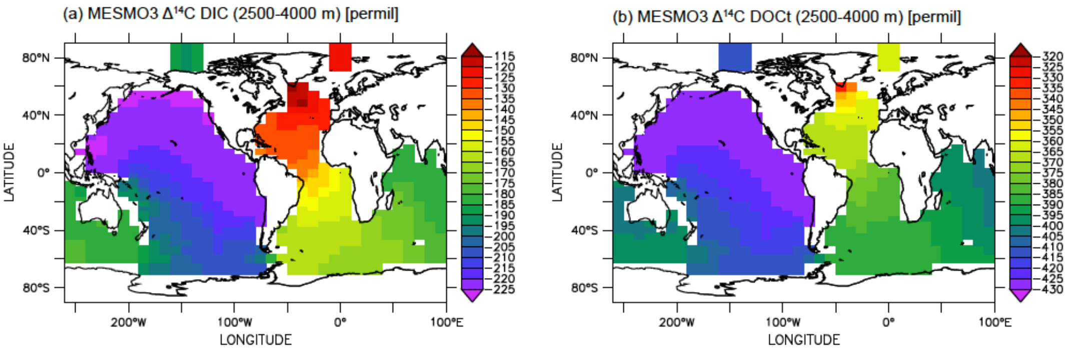

Figure 10. $\Delta^{14}C$ of deep ocean DIC (a) and DOC_t (b) from the DOM_R-enabled MESMO 3 *LV* run. Vertical average over 2500-4000 m water depth. Unit = ‰.

Table 1. Summary of MESMO Development

Model (run ID)	Biogeochemical features	Physical features
MESMO3 (190917c)	3 PFTs: Eu, Cy, and Dz Uptake C:N:P=f(PO_4, NO_3, T, PAR) by power law N cycle (N-fixation, denitrification) OM remineralization=f(O_2, T) CaCO3 production by Eu RNPG: competition w/in single Eu PFT fDOM=f(T) *Optional*: Alternative uptake C:N:P by cell quota *Optional*: DOC, DOP, DON, DOFe (semi-labile) *Optional*: DOCr, DOPr, DONr (refractory)	
MESMO 2 (120531a)	Nutrients= PO_4, NO_3, CO_2, Fe, Si 2 PFTs: LG, SM Si cycle (Si, ^{30}Si) Fe cycle (Fe', FeL) Uptake C:Fe=(FeT) Uptake Si:N=f(FeT) by LG CaCO3 production by SM	Seasonal winds
MESMO1 (090309a)	J_{prod}=(PAR, nutrients, T, MLD) Nutrients=PO_4, NO_3, CO_2(aq) DOC (semi-labile) fDOM=0.67	16 vertical levels Arctangent $K_v(z)$ Seasonal PAR

PFT=phytoplankton functional types. MESMO2 PFTs are LG=large/diatoms and SM=small. MESMO3 PFTs are Eu=eukaryotes, Cy=cyanobacteria, and Dz=diazotrophs. OM=organic matter. RNPG=residual nitrate potential growth. T=temperature. PAR=photosynthetically available radiation. fDOM=fraction of NPP routed to dissolved organic matter (DOM). The two types of DOM are semi-labile (DOC, DOP, DON, and DOFe) and refractory (DOCr, DOPr, and DONr). Carbon isotopes (^{12}C, ^{13}C, and ^{14}C) are calculated separately for DOC and DOCr.

Table 2. MESMO 3 Biogeochemical Model Parameters Values

Table 2a. Phytoplankton nutrient uptake

	Parameter	Description	Unit	MESMO 2	MESMO3
	LP/Eukaryotes				
	τ	Optimal uptake	yr^{-1}	0.01	0.002
	K_{PO4}	PO_4 half saturation const	µmol kg^{-1}	0.39	0.120
	K_{NO3}	NO_3 half saturation const	µmol kg^{-1}	5.00	3.4
	K_{CO2}	CO_2 (aq) half saturation const	µmol kg^{-1}	0.925	0.925
	K_{Fe}	FeT half saturation const	nmol kg^{-1}	0.10	0.30
	$K_{Si(OH)4}$	$Si(OH)_4$ half saturation const	µmol kg^{-1}	1.0	1.0
	SM/Cyanobacteria				
	τ	Optimal uptake	yr^{-1}	0.16	0.04
	K_{PO4}	PO_4 half saturation const	µmol kg^{-1}	0.03	0.012
	K_{NO3}	NO_3 half saturation const	µmol kg^{-1}	0.50	2.0
	K_{CO2}	CO_2 (aq) half saturation const	µmol kg^{-1}	0.075	0.075
	K_{Fe}	FeT half saturation const	nmol kg^{-1}	0.01	0.008
	Diazotrophs				
	τ	Optimal uptake	yr^{-1}	-	0.2
	K_{PO4}	PO_4 half saturation const	µmol kg^{-1}	-	0.300
	K_{NO3}	NO_3 half saturation const	µmol kg^{-1}	-	0.4
	K_{NO3_Nfix}	K_{NO3} for N-fixation	µmol kg^{-1}	-	2.0
	K_{CO2}	CO_2 (aq) half saturation const	µmol kg^{-1}	-	0.075
	K_{Fe}	FeT half saturation const	nmol kg^{-1}	-	0.030

Table 2b. Power law model of flexible C:N:P stoichiometry

	Parameter	Description	Unit	MESMO 2	MESMO3
	$[PO_4]_0$	Reference $[PO_4]$	µmol kg^{-1}	-	0.57
	$[PO_4]_0$	Reference $[NO_3]$	µmol kg^{-1}	-	5.7
	T_0	Reference temperature	°K	-	291
	I_0	Reference light level	W m-2	-	70
	Eukaryotes				
	[P:C]0	Reference P:C molar ratio	-	-	11.6
	[N:C]0	Reference N:C molar ratio	-	-	151.0
	$s^{P:C}_{PO4}$	Sensitivity of P:C to $[PO_4]$	-	-	0.58
	$s^{N:C}_{NO3}$	Sensitivity of N:C to $[NO_3]$	-	-	0.22
	$s^{N:C}_{I}$	Sensitivity of N:C to light	-	-	-0.05
	Cyanobacteria				
	[P:C]0	Reference P:C molar ratio	-	-	6.3
	[N:C]0	Reference N:C molar ratio	-	-	151.0
	$s^{P:C}_{PO4}$	Sensitivity of P:C to $[PO_4]$	-	-	0.28
	$s^{N:C}_{NO3}$	Sensitivity of N:C to $[NO_3]$	-	-	0.22
	$s^{P:C}_{T}$	Sensitivity of P:C to temperature	-	-	-8.0
	$s^{N:C}_{I}$	Sensitivity of N:C to light	-	-	-0.05
	Diazotrophs				
	[P:C]0	Reference P:C molar ratio	-	-	6.3
	[N:C]0	Reference N:C molar ratio	-	-	151.0
	$s^{P:C}_{PO4}$	Sensitivity of P:C to $[PO_4]$	-	-	0.28
	$s^{P:C}_{T}$	Sensitivity of P:C to temperature	-	-	-8.0
	$s^{N:C}_{I}$	Sensitivity of N:C to light	-	-	-0.05

Sensitivity factors not listed here have a value of zero (e.g., $s^{N:C}_{PO4}=0$; thus the environmental driver PO_4 does not drive the N:C ratio.

Table 2c. Iron uptake stoichiometry

	Parameter	Description	Unit	MESMO 2	MESMO3
	LP/Eukaryotes				
	$[C:Fe]_{min}$	Minimum C:Fe molar ratio	-	0	15,000:1
	$[C:Fe]_{ref}$	Scaling C:Fe molar ratio	-	103,684:1	115,623:1
	$s^{Fe:C}$	Power law exponent	-	-0.4225	-0.65
	SM/Cyanobacteria				
	$[C:Fe]_{min}$	Minimum C:Fe molar ratio	-	0	20,000:1
	$[C:Fe]_{ref}$	Scaling C:Fe molar ratio	-	103,684:1	31,805:1
	$s^{Fe:C}$	Power law exponent	-	-0.4225	-0.65
	Diazotrophs				
	$[C:Fe]_{min}$	Minimum C:Fe molar ratio	-	-	20,000:1
	$[C:Fe]_{ref}$	Scaling C:Fe molar ratio	-	-	31,805:1
	$s^{Fe:C}$	Power law exponent	-	-	-0.65

Table 2d. Parameters related to POM, DOM, $CaCO_3$, and Opal

	Parameter	Description	Unit	MESMO 2	MESMO3
Particle sinking					
	w	sinking speed	$m\ d^{-1}$	30	120
POM remineralization					
	V_{POM}	Base remineralization rate	d^{-1}	0.1	0.16
	k_R	Temperature sensitivity	-	0.69	0.69
	K_{O2}	O2 half saturation constant	$\mu mol\ kg^{-1}$	-	30
DOM remineralization					
	τ_{sl}	DOM_{sl} decay time scale	yr^{-1}	0.5^{-1}	1.5^{-1}
	τ_{bg}	DOM_r background decay time scale	yr^{-1}	-	$16{,}000^{-1}$
	τ_{photo}	DOM_{sl} photodegradation time scale	yr^{-1}	-	70^{-1}
	τ_{vent}	DOM_{sl} vent decay time scale	yr^{-1}	-	$>\Delta t^{-1}$
	H_{flux}	Global annual seawater flux through hydrothermal vents	$kg\ yr^{-1}$	-	4.8×10^{16}
$CaCO_3$ remineralization					
	V_{CaCO3}	Base remineralization rate	d^{-1}	0.05	0.05
	k_R	Temperature sensitivity	-	0.69	0.69
Opal remineralization					
	V_{Opal}	Base remineralization rate	d^{-1}	0.01	0.01

Table 2e. Nitrogen and iron cycles

	Parameter	Description	Unit	MESMO 2	MESMO3
N cycle					
	K_{N2}	N_2 half saturation constant in I_{NO3}	μmol kg^{-1}	-	0.48
	k_D	Scaling constant in eq 62	μmol kg^{-1}	-	1.5
Fe cycle					
	K_{ligand}	Cond. stability of constant	-	$1.25x10^{11}$	$1.0x10^{11}$
	τ_{sc}	Fe scavenging rate scale factor	-	0.7	0.7
	K_0	Base Fe scavenging rate	d^{-1}	0.079	0.079

Table 3. Key Biogeochemical Diagnostics

	Diagnostics	Unit	Constraint	MESMO 2 (120531a)	MESMO 3 (190917a)
Phytoplankton community/Bulk					
	NPP	Pg C y^{-1}	30-70	36.0[a]	34.6
	POC export	Pg C y^{-1}	4-10	11.9	9.4
	DOC export	Pg C y^{-1}	0.4-2	0.4	0.5
	Opal export	Tmol Si y^{-1}	70-185	130	128
	CaCO$_3$ export	Pg C y^{-1}	0.4-1.8	1.0	0.6
	fDOM	%		0.66	0.71
	N fixation	Tg N y^{-1}	80-200	-	109
	Denitrification	Tg N y^{-1}	60-150	-	109
	Uptake C:N:P	molar ratio	146:20:1	117:16:1	146:19:1
	Export C:N:P	molar ratio	117:16:1	117:16:1	113:16:1
	Deep O$_2$	μmol kg^{-1}	169	179	157
LP/Eukaryotes					
	Uptake C:N:P	molar ratio		117:16:1	102:14:1
	POC export	Pg C y^{-1}		8.7	3.6
	Abundance	%		73[b]	39
SM/Cyanobacteria					
	Uptake C:N:P	molar ratio		117:16:1	198:23:1
	POC export	Pg C y^{-1}		3.2	4.9
	Abundance	%		27[b]	52
Diazotrophs					
	Uptake C:N:P	molar ratio		-	213:32:1
	POC export	Pg C y^{-1}		-	0.8
	Abundance	%		-	9

[a]NPP for MESMO 2 was unavailable as a model output and therefore estimated from POC and fDOM=0.66. [b]The calculation of the PFT abundance requires NPP in terms of P. NPP was unavailable as a model output for MESMO 2, so PFT % was estimated from POC export.

References for independent constraints: (1) global NPP (Carr et al., 2006); (2) global POC export (DeVries and Weber, 2017); (3) global DOC export assumed to be 20% of total carbon export (Hansell et al., 2009; Roshan and DeVries, 2017); (4) global opal (Dunne et al., 2007); (5) global CaCO$_3$ export (Berelson et al., 2007); (6) global N fixation and denitrification rates (Landolfi et al., 2018); (7) uptake C:N:P ratio is based on POM measurements (Martiny et al., 2013); (8) export C:N:P ratio is assumed to equal the

https://doi.org/10.5194/gmd-2020-408
Preprint. Discussion started: 6 January 2021

subsurface remineralization ratio (Anderson and Sarmiento, 1994); (9) Deep O_2 from WOA13 below 100 m (Garcia et al., 2013).